10.37965/jdmd.2026.1308

Management of Thermal Comfort in Smart Homes: Assessing Radiator Performance under Controlled Seasonal Ventilation and Humidity Conditions

Aminu E. Isiyaku, Rakesh Mishra
School of Computing and Engineering,
University of Huddersfield, Huddersfield, HD1 3DH, UK
*Corresponding author. aminu.isiyaku@hud.ac.uk

Received 04 April, 2026 | Revised 04 June,2026 | Accepted 09 June, 2026 | Posted Online 11 June, 2026

Abstract: This study evaluates the thermal comfort performance of a conventional hydronic radiator system in a smart home under varying seasonal, ventilation and humidity conditions. A transient Reynolds-Averaged Navier-Stokes Computational Fluid Dynamics (RANS-CFD) model, partially supported by sensor-based microclimate measurements, was used to simulate twelve controlled scenarios based on representative summer and winter outdoor boundary temperatures of 20 °C and 5 °C, respectively, with open- and closed-window conditions and relative humidity levels of 30%, 50% and 70%. Thermal comfort was assessed using the Predicted Mean Vote (PMV) and Predicted Percentage of Dissatisfied (PPD) indices. The results show that the radiator system maintained slightly warm but near-acceptable comfort in summer closed-window cases, but failed to achieve acceptable comfort in winter, even with windows closed. Open-window conditions caused substantial comfort deterioration through ventilation-driven heat loss, with the winter open-window cases producing severe cold discomfort (PMV < −2.18, PPD > 82%). Within the adopted air-temperature-based approximation of mean radiant temperature, regression analysis showed that air temperature was the dominant comfort-related variable, while relative humidity had only a weak linear influence. CFD-based spatial analysis predicted clear thermal non-uniformity, particularly in the stair/landing region, where buoyancy-driven warm-air transport and local heat accumulation produced persistent anomaly. Overall, the findings indicate that effective smart radiator control in modern dwellings should prioritise window-state awareness, zonal interpretation and spatial comfort mapping, while treating humidity as a secondary comfort variable.

Keywords: Thermal comfort, Smart home, Radiator heating, CFD simulation, PMV-PPD, Humidity effects, Ventilation

10.37965/jdmd.2026.1308

I. INTRODUCTION

Thermal comfort in buildings is an important component of indoor environmental quality because people spend some 85-90% of their time in homes, workplaces and other enclosed spaces [1]. A comfortable indoor climate has a strong connection with occupant's health, wellbeing and productivity [2], so poor comfort can easily turn into discontent and less performance. In homes and smart homes, space heating and cooling consume a large portion of the household's energy consumption and, at the level of the built environment, buildings are responsible for around 30-40% of the globe's final energy consumption and a comparable share of energy-related emissions.[3][4]. This has led to increased regulation and design standards to improve the energy performance of buildings whilst maintaining a recognised comfort level inside the building.

A key instrument to express thermal comfort is the Predicted Mean Vote (PMV) model and its equivalent Predicted Percentage of Dissatisfied (PPD) to estimate the average thermal sensation of some group of people and the probable percentage that will be uncomfortable in "moderate" indoor environments. ISO 7730 and EN 16798 PMV/PPD are embedded in standards as a main basis for defining acceptable conditions [5]. However, the PMV model assumes steady state conditions and a homogenous indoor environment, while in real dwellings the environment may be dynamic and may not be homogeneous - for instance, air is warmer near a radiator and cooler near a window. Researchers have therefore coupled multi-segment human thermoregulation models with Computational Fluid Dynamics (CFD) to investigate the transient and spatially varying effects on different parts of the body and local comfort values, i.e. beyond a single PMV value.

Despite these limitations, PMV/PPD are today still the principal global measures of overall comfort and are very popular in CFD-based studies. Slimani et al. (2025) using CFD and field measurements, analyse an office building in Béchar, Algeria and find an initial summer PMV of about +2.33 (very warm) with >65% of occupants dissatisfied and after optimisation of the envelope PMV is within the −0.5 to +0.5 comfort band and PPD is about 30-57% and strong agreement between CFD and field measurements is found (r approx. 0.94) [6]. This is both an example of the usefulness of PMV/PPD as performance indicators and the potential of CFD to be used for reliable spatial prediction of comfort.

Hydronic panel radiators are one of the most common heating terminals in the residential sector due to their simplicity, robustness and ease of installation, suitable for installation in new and existing buildings [7]. Previous work within the Huddersfield Smart House research programme has also examined thermal comfort in a radiator-heated smart-house setting, demonstrating the suitability of the testbed for evaluating heat distribution and comfort response under domestic heating conditions [8]. They are normally mounted under windows so that the warm convective plume which rises from the radiator can intercept the cold downdraught which is generated and forms along the glazing which would otherwise sink to the floor and cause "cold feet" discomfort near the ankles [9]. A variety of experimental and numerical studies have been done on the interaction of radiator plumes and downdraughts from windows. Most recently

the temperature range of radiator operation has been optimised so that downdraughts from a cold window are neutralised without overheating the room by using a response surface model relating radiator surface temperature, outdoor climate and envelope characteristics to room operative temperature and the window-air temperature difference (Wu, 2024) [1]. By adjusting the average temperature of the radiators, they were able to keep the operative temperature in the comfort band while they almost eliminated cold draught hours at the window, reducing the occurrence of draught by around an order of magnitude. This indicates that careful control of radiator output can be used to improve comfort and avoid unnecessary heat loss.

Radiator heating also influences the vertical profile of temperature in a room. This effect is particularly relevant in the Huddersfield Smart House, where earlier computational analysis of radiator operation showed that radiator-driven indoor air movement can influence local airflow structures and temperature distribution within the dwelling [10]. Since warm air rises, the air at head level is generally warmer than the air at ankle level. Standards such as ISO 7730 and ASHRAE 55 recommend that the vertical air-temperature difference between head and ankle levels should not exceed about 3 K in the occupied zone to avoid local discomfort [5]. Well-designed radiator systems in small rooms can often maintain this difference within approximately 1-2 K, although this may be affected by room layout and ventilation strategy. A recent CFD analysis of a naturally ventilated, radiator-heated office showed that improperly located ventilation openings can cause the heat to be trapped close to the ceiling resulting in large stratification and causing the radiators to work harder, while inlet and outlet locations that allow for vertical mixing allow for both reduced energy consumption and a more uniform temperature distribution in the occupied zone [11]. Wu et al. (2021) used thermal image velocimetry to measure the flow of air above a radiator and proposed a momentum-balance method to judge when the radiator is "overheating" that is, when the convective plume more than compensates the downdraught and drives room temperatures above the comfort range [9]. Such methods are directly relevant for demand-responsive radiator controls for smart houses.

CFD has become an important tool in the analysis of indoor environments because it can resolve the temperature, air speed and turbulence throughout space, rather than at a few sensor points. It is widely used together with comfort models, such as PMV/PPD and the Draught Rate (DR) index, for mapping comfort in space and time. DR is a prediction of the percentage of occupants likely to be dissatisfied due to draught at a particular location depending on local air temperature, mean speed and turbulence intensity, and is widely recommended as a local discomfort index in ISO 7730 and EN 16798 [5]. Markov et al. (2020) applied unsteady CFD and time-resolved measurements in a university classroom and demonstrated that large-scale airflow variations at low frequencies can make DR vary drastically with time; when steady RANS simulations or short-term measurements are considered, draught discomfort can be underestimated severely [12]. They found that effective measurement of draught in such spaces needs time-resolved CFD or protracted surveillance and not merely multiple snapshot values of draught.

CFD is also a very useful optimisation tool. For example, Slimani et al. (2025) applied a combined Building Energy Simulation-CFD method on an Algerian office, in order to test various envelope improvements and quantify their impact on

the PMV, PPD and energy demand, while other studies have varied size and position of natural ventilation openings in radiator-heated offices and optimised configurations that keep PMV close to zero, DR below about 10% and heating demand low.[6][9]. Zhou et al (2023) have also applied CFD-based multi-criteria optimisation for impinging jet ventilation, where PMV is used as an overall comfort objective, and DR is used as a local draught comfort objective, and demonstrates how supply location and flow rate can be adjusted to balance uniform comfort and low energy use [13]. CFD studies of personalised and stratum ventilation systems have also shown that supplying fresh air directly to the occupied zone can improve perceived comfort and reduce the need to condition the entire room volume. However, some studies also report increased vertical temperature gradients, which may need to be managed to avoid local discomfort [12].

Thermal comfort itself is dependent on six main factors: air temperature, mean radiant temperature, air velocity, humidity, clothing insulation and metabolic rate. Recent domestic indoor comfort research has similarly shown that radiator surface temperature, ambient conditions, ventilation and relative humidity can jointly influence thermal comfort outcomes in residential spaces [14]. In practice PMV/PPD are the only two major overall indices that remain for the standards for offices and homes, with a recommended comfort band of PMV between -0.5 and +0.5 (about < 10% PPD). ISO 7730 and EN 16798, however, also contain limits of local discomfort factors such as draught, vertical air temperature difference, floor surface temperature and radiant temperature asymmetry [5]. Typical guidance is that the temperature difference between ankle (0.1 m) and head (1.1 m) in the occupied zone should not exceed about 3 K, that floor temperature should stay between roughly 19-29 °C, that radiant asymmetry (for example between a cold window and warm interior) should be below about 5 °C, and that acceptable DR values are usually below 15-20%.

Vertical stratification is a local parameter of particular importance in heated rooms. Radiator heating tends to give warmer air towards the ceiling and cooler air towards the floor, but floor heating may result in warmer air towards the feet. Using large field datasets from the Chinese Thermal Comfort Database, Du et al. (2022) compared radiant and convective systems and found that during heating, radiant systems tended to have slightly higher air temperatures near the floor but that neutral temperature differences between the two systems were within about 1.1 ºC - narrower than the limits suggested by national standards [13]. They also demonstrated that vertical temperature difference, radiant asymmetry, air velocity and floor temperature may all be kept within comfort limits when systems are well designed and controlled.

Mean radiant temperature (MRT) and its uniformity MRT are also of great importance. A person sitting next to a large and cold window may feel uncomfortable, even if air temperature is nominally acceptable for a person, because the cold surface reduces the person's MRT. Radiation above the window increases the MRT by warming the surfaces close to the window, and reduces the radiant asymmetry, which is one of the reasons why this configuration is so widespread [8]. Laouadi 2004 developed a radiant heating and cooling model for energy simulation in buildings and established that operative temperature (which is the average of air temperature and MRT) is a better single descriptor of comfort in non-uniform environments[15]. Later work on low temperature radiant systems, like Bojić et al. (2013), confirmed that the panel systems can

provide good comfort at lower air temperature by increasing MRT, improving energy performance compared with traditional radiator systems [16]. Wu (2024) therefore made the operative temperature the primary comfort measure in radiator optimisation so that it fell within a typical winter comfort band of around 20-24°C [1].

In smart homes, the best current practice is to use a combination of sensors, control algorithms and physical design to maintain global as well as local comfort. Modern sensor networks and IoT platforms can monitor temperature, humidity, CO_2 and particulates on a continuous basis, as well as feed the information into smart heating controls [16][17]. Meanwhile, CFD modeling of indoor microclimates, and sophisticated comfort models (PMV/PPD and local indices such as DR, stratification, and radiant asymmetry) enable the designer modelling of radiator layouts, window designs and ventilation planning, as well as to devise rules of control which vary according to changes in outside weather or window opening. Combined, the above developments enable it to be possible to run radiator systems within a smart home such that overall comfort goals are achieved and local issues such as cold window draughts, over-large vertical gradients or hot ceilings are avoided.

Against this background, the present study assesses the thermal comfort performance of a conventional hydronic radiator system in the Huddersfield Smart House, a two-bedroom duplex smart-home testbed instrumented with sensors for temperature, relative humidity, carbon dioxide (CO_2), particulate matter ($PM_{2.5}$) and air speed. Radiators were represented at a surface temperature of approximately 60 °C, reflecting typical domestic operation. Twelve transient CFD scenarios were considered: six summer cases (S1-S6) with an outdoor temperature of 20 °C and six winter cases (W1-W6) with an outdoor temperature of 5 °C. For each season, window state was varied between closed and open conditions, while outdoor relative humidity was imposed at 30%, 50% and 70%. To capture vertical non-uniformity in the occupied zone, comfort-related variables were extracted at the forehead, chest, knee and ankle levels of the mannequins.

The central research question of this study is: How effectively can a conventional radiator heating system maintain thermal comfort in a smart home under changing seasonal, window-opening and humidity conditions? The study addresses this question by combining sensor-supported validation with whole-house transient CFD analysis and PMV/PPD-based comfort assessment.

Accordingly, the aim of this study is to quantify how season, window state and relative humidity influence thermal comfort in a radiator-heated smart-home environment, while identifying spatial non-uniformities that are not captured by whole-house average conditions. Although CFD modelling and PMV/PPD-based comfort assessment are well established, fewer studies have applied them together in a validated whole-house smart-home radiator case with explicit attention to vertical body-height comfort, transitional zones and control-relevant spatial anomalies. The uniqueness of the present work is therefore not the use of CFD or PMV/PPD alone, but their combined application to a sensor-instrumented residential testbed under a controlled twelve-scenario framework.

The study makes four main contributions. First, it provides a whole-house transient CFD-based comfort assessment for a sensor-instrumented smart-home testbed, including multiple rooms and body-level extraction heights. Second, it compares twelve controlled scenarios covering seasonal boundary conditions,

open- and closed-window operation, and three relative humidity levels. Third, it identifies the dominant influence of air temperature and window state on PMV/PPD outcomes within the tested range. Fourth, it predicts a persistent stair/landing thermal anomaly within the CFD framework, showing the importance of zonal interpretation in multi-level radiator-heated dwellings.

B. Case Study: Huddersfield Smart House. The Huddersfield Smart House was used as a representative low-rise UK residence for combined experimental and computational analysis. The same facility has also been used in related smart-home thermal comfort research, where sensor-supported environmental monitoring, CFD-based assessment and comfort indicators were applied to evaluate indoor thermal performance in a residential testbed [19]. The property is a duplex with an open-plan living, dining and kitchen area on the ground floor, and two bedrooms and a bathroom on the upper floor. Space heating is provided by hydronic panel radiators installed in the regularly occupied rooms.

To capture the thermal environment at occupant level, measurements were considered at four anatomical heights above the finished floor: forehead (1.62 m), chest (1.30 m), knee (0.42 m) and ankle (0.07 m). These locations were used to assess vertical stratification and to support PMV/PPD calculations. Experimental measurements used for validation were obtained in the living room and kitchen, while the CFD analysis extended the same sampling strategy across the wider house, including the living area, kitchen, stair landing and bedrooms. This arrangement enabled both local and whole-house assessment of thermal comfort non-uniformity, consistent with recent CFD-experimental studies showing that locally heated residential spaces can develop significant ankle-to-head temperature gradients that affect occupant comfort [20].

Fig. 1 presents the building geometry, internal zoning, radiator and mannequin locations and body-level sampling configuration. Fig. 2 illustrates the mannequin model and the fixed anatomical sampling points used for extraction of air temperature, air velocity and humidity-related variables for comfort assessment.

10.37965/jdmd.2026.1308

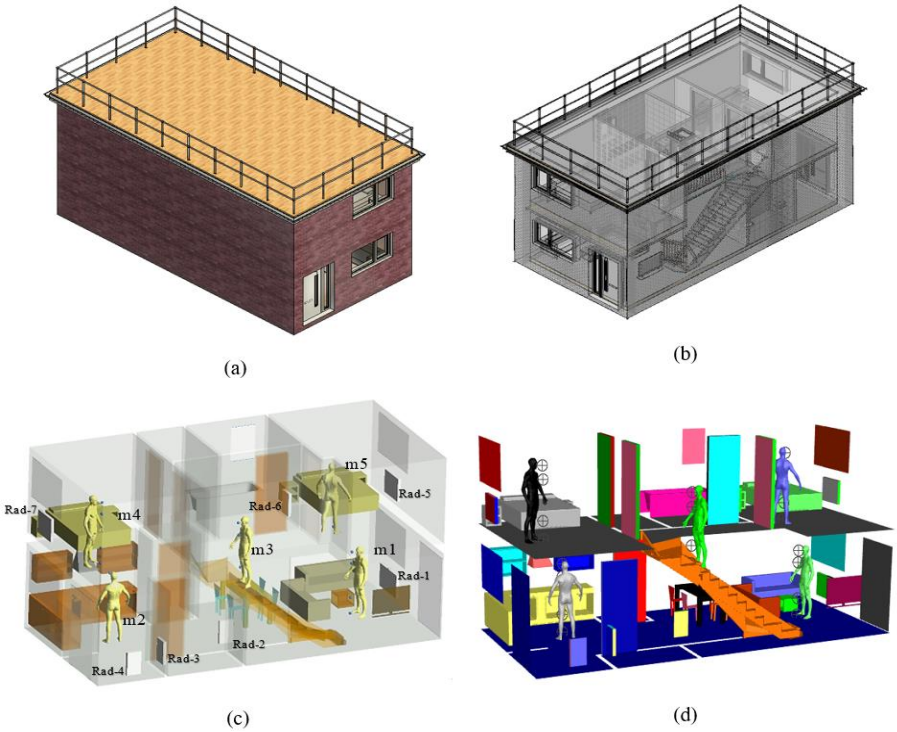

Fig. 1. Smart House geometry and mannequin configuration: (a) architectural model, (b) 3D X-ray view, (c) radiator and mannequin placement and sampling levels, (d) Views with body measurement points.

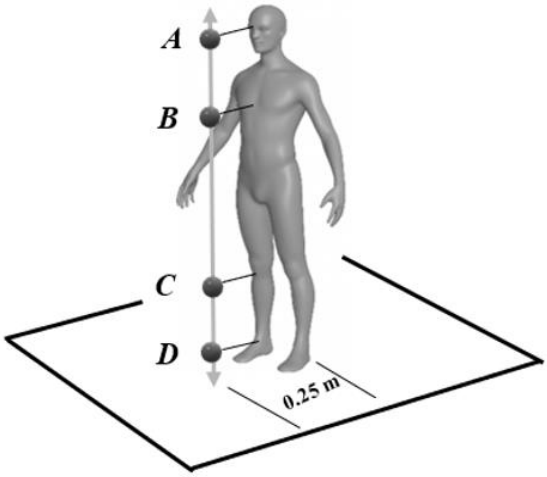

Label	Body Landmark	Standard Height from Floor (m)
A	Forehead	1.62
B	Chest	1.30
C	Knee	0.42
D	Ankle	0.07

Fig. 2. CFD mannequin with anatomical sampling heights (forehead, chest, knee, ankle).

II. METHODOLOGY

This study uses an experimentally supported Computational Fluid Dynamics (CFD) framework to evaluate the thermal performance of a hydronic radiator system in a smart-home environment under controlled seasonal, ventilation and humidity conditions. The methodology combines transient numerical simulation with PMV/PPD-based thermal comfort assessment using recognised international comfort standards. The

experimental measurements were used to support point-based comparison of selected comfort variables, while the wider airflow and temperature distributions are interpreted as CFD-predicted spatial fields.

A. NUMERICAL MODEL AND SOLVER CONFIGURATION

The indoor airflow, heat transfer and water-vapour transport were simulated using a three-dimensional transient Reynolds-Averaged Navier-Stokes (RANS) formulation. Buoyancy effects were represented using the Boussinesq approximation, which assumes constant density except in the gravitational body-force term. This approach is suitable for indoor mixed-convection flows where temperature-induced density differences drive buoyant motion, but the overall density variation remains small [21][22][23].

The RNG k-ε turbulence model with enhanced wall treatment was used to close the RANS equations. This model was selected as a practical engineering RANS closure for the whole-house transient simulations because it provides stable and computationally affordable prediction of mixed-convection indoor airflow, including radiator-driven buoyant plumes, weak recirculation and local shear regions near walls, openings and mannequin surfaces [21][23][24]. The RANS formulation therefore accounts for the Reynolds stresses through the Boussinesq eddy-viscosity hypothesis rather than treating the flow as laminar.

However, the use of RNG k-ε also imposes modelling limitations. As an eddy-viscosity RANS model, it assumes an isotropic turbulent viscosity and does not explicitly resolve all low-Reynolds-number transitional structures, anisotropic turbulence, local separation or detailed cold-window downdraught behaviour. These effects may be important in strongly stratified indoor natural-convection regions. Therefore, the turbulence model was considered suitable for comparative whole-house comfort assessment, but not for high-fidelity resolution of all local boundary-layer and downdraught structures.

Simulations were performed in ANSYS Fluent 2022 R2. Second-order upwind discretisation was used for the momentum, energy and turbulence equations, while PRESTO! pressure interpolation was adopted to improve pressure treatment in buoyancy-affected indoor flow. A fixed time step of 30 s was used for all transient scenarios, and numerical stability was maintained with a Courant number below 1.0. Convergence was monitored using scaled residual targets of 10^{-6} for the energy equation and 10^{-4} for the continuity, momentum, turbulence and species equations [23].

The time-averaged continuity equation for incompressible indoor airflow is [21][22]:

$$\frac{\partial \bar{u_\iota}}{\partial x_i} = 0$$

where $\bar{u_\iota}$ is the mean velocity component in the x_i direction.

The RANS momentum equation with buoyancy is written as [21][22][23]:

$$\frac{\partial \bar{u_\iota}}{\partial t} + \bar{u_\jmath}\frac{\partial \bar{u_\iota}}{\partial x_j} = -\frac{1}{\rho_0}\frac{\partial \bar{p}}{\partial x_i} + \frac{\partial}{\partial x_j}\left[(\nu+\nu_t)\left(\frac{\partial \bar{u_\iota}}{\partial x_j}+\frac{\partial \bar{u_\jmath}}{\partial x_i}\right)\right] + g_i\beta\left(\bar{T}-T_{ref}\right)$$

where ρ_0 is the reference density, $\bar{p}$ is the mean pressure, ν is the molecular kinematic viscosity, ν_t is the turbulent kinematic viscosity, g_i is the gravitational acceleration component, β is the thermal expansion coefficient, $\bar{T}$ is the mean air temperature and T_{ref} is the reference temperature. The

pressure-gradient term is therefore expressed in the dimensionally consistent form $-\frac{1}{\rho_0}\nabla\bar{p}$. The Reynolds stress tensor is closed using the Boussinesq eddy-viscosity approximation [21][22][23]:

$$-\rho_0\overline{u_i'u_j'} = \mu_t\left(\frac{\partial\bar{u}_i}{\partial x_j}+\frac{\partial\bar{u}_j}{\partial x_i}\right)-\frac{2}{3}\rho_0 k\delta_{ij}$$

where μ_t is the turbulent dynamic viscosity, k is the turbulent kinetic energy and δ_{ij} is the Kronecker delta.

The turbulent viscosity in the RNG $k-\varepsilon$ model is given by [23][24]:

$$\mu_t = \rho_0 C_\mu \frac{k^2}{\varepsilon}$$

where ε is the turbulence dissipation rate and C_μ is the RNG model constant.

The transport equation for turbulent kinetic energy is:

$$\frac{\partial k}{\partial t}+\bar{u_j}\frac{\partial k}{\partial x_j} = \frac{\partial}{\partial x_j}\left[\left(\nu+\frac{\nu_t}{\sigma_k}\right)\frac{\partial k}{\partial x_j}\right]+P_k+P_b-\varepsilon$$

The transport equation for the dissipation rate is:

$$\frac{\partial \varepsilon}{\partial t}+\bar{u_j}\frac{\partial \varepsilon}{\partial x_j} = \frac{\partial}{\partial x_j}\left[\left(\nu+\frac{\nu_t}{\sigma_\varepsilon}\right)\frac{\partial \varepsilon}{\partial x_j}\right] + C_{1\varepsilon}\frac{\varepsilon}{k}(P_k+C_{3\varepsilon}P_b)-C_{2\varepsilon}\frac{\varepsilon^2}{k} - R_\varepsilon$$

where P_k is the production of turbulent kinetic energy due to mean velocity gradients, P_b is the buoyancy production term, σ_k and σ_ε are turbulent Prandtl numbers for k and ε, and R_ε is the additional strain-rate-dependent term in the RNG $k-\varepsilon$ formulation.

The mean energy equation was solved as [22][23]:

$$\frac{\partial \bar{T}}{\partial t}+\bar{u_j}\frac{\partial \bar{T}}{\partial x_j} = \frac{\partial}{\partial x_j}\left[\left(\alpha+\frac{\nu_t}{Pr_t}\right)\frac{\partial \bar{T}}{\partial x_j}\right]+\frac{S_h}{\rho_0 c_p}$$

where α is the molecular thermal diffusivity, Pr_t is the turbulent Prandtl number, S_h is the heat-source contribution from radiator boundary heating and c_p is the specific heat capacity of air.

Water-vapour transport was represented using a passive scalar species equation [22][23]:

$$\frac{\partial \bar{Y}_v}{\partial t}+\bar{u_j}\frac{\partial \bar{Y}_v}{\partial x_j} = \frac{\partial}{\partial x_j}\left[\left(D_v+\frac{\nu_t}{Sc_t}\right)\frac{\partial \bar{Y}_v}{\partial x_j}\right]+S_v$$

where $\bar{Y}_v$ is the mean water-vapour mass fraction, D_v is the molecular diffusivity of water vapour in air, Sc_t is the turbulent Schmidt number and S_v is the vapour source term. Relative humidity was then obtained from the local temperature and water-vapour field for use in the PMV/PPD comfort calculation.

Radiative heat transfer was not explicitly solved in the present CFD model. The radiators were represented as isothermal heating surfaces, and their effect on the indoor environment was resolved through the energy equation, buoyancy-driven airflow and convective heat transfer to the surrounding air. Therefore, long-wave surface-to-surface radiation exchange between radiators, walls, glazing and mannequins were not included. No Discrete Ordinates (DO), Surface-to-Surface (S2S), or P1 radiation model was activated in ANSYS Fluent. Consequently, local incident radiative heat fluxes and spatially resolved mean radiant temperature fields were not directly available from the CFD solution [23].

B. COMPUTATIONAL DOMAIN, MESH AND MESH SENSITIVITY

A poly-hexcore meshing strategy was employed for the whole-house computational domain. Local mesh refinement was applied around the radiator surfaces, ventilation openings and mannequin bodies to improve the resolution of local thermal and flow gradients. Prism inflation layers were applied to the main wall-bounded and thermally important surfaces, including the radiators, windows, floor, internal walls and

mannequin surfaces, to improve near-wall resolution. The adopted production mesh contained approximately 4.2 million hybrid elements.

A mesh-sensitivity assessment was carried out using the representative summer closed-window 30% RH scenario (S1). This case was selected because it represents a low-air-movement closed-window condition and because its mean occupied-zone velocity was very close to the overall mean velocity obtained across the closed-window relative-humidity cases. Three mesh densities were considered: coarse, medium and fine. The medium mesh corresponds to the adopted production mesh used for the main simulations.

For each mesh, the representative occupied-zone temperature was calculated from the body-level extraction points across the five mannequin locations. The m3-ankle value was excluded from the temperature average because it had already been identified as a local stair/landing anomaly. For the production mesh, this gave a representative occupied-zone temperature of 26.49 °C, with a corresponding mean occupied-zone velocity of 0.0896 m/s and an average PMV of +0.45 for the same scenario.

The mesh comparison was based on representative comfort-related outputs, including occupied-zone air temperature, air velocity and PMV. The percentage difference between each mesh and the fine mesh was calculated as [25][26]:

$$\Delta Q(\%) = \left| \frac{Q_{\text{mesh}} - Q_{\text{fine}}}{Q_{\text{fine}}} \right| \times 100$$

where Q_{mesh} is the value predicted by the coarse or medium mesh, and Q_{fine} is the corresponding value predicted by the fine mesh. For temperature and velocity, the percentage difference was reported. For PMV, the absolute difference was reported because PMV is a dimensionless comfort index rather than a directly dimensional flow variable:

$$\Delta PMV = \left| PMV_{\text{mesh}} - PMV_{\text{fine}} \right|$$

Table 1. Mesh-sensitivity assessment for the representative summer closed-window 30% RH scenario (S1).

Mesh level	Number of elements	Representative occupied-zone temperature (°C)	Representative occupied-zone velocity (m/s)	Average PMV (-)	Difference from fine mesh
Coarse	1,520,000	25.70	0.1080	+0.34	ΔT = 3.38%, Δv = 22.73%, ΔPMV = 0.12
Medium / production mesh	4,200,000	26.49	0.0896	+0.45	ΔT = 0.41%, Δv = 1.82%, ΔPMV = 0.01
Fine / refined mesh	8,030,000	26.60	0.0880	+0.46	Reference

10.37965/jdmd.2026.1308

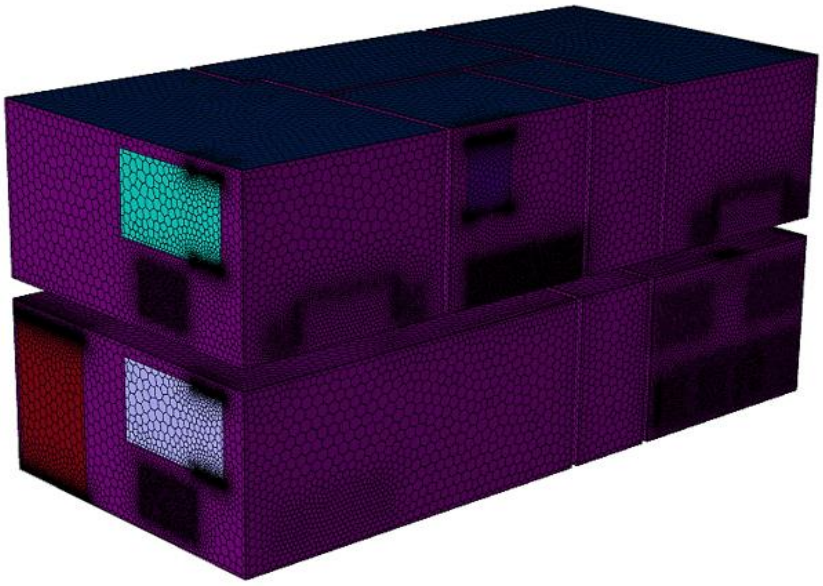

(a)

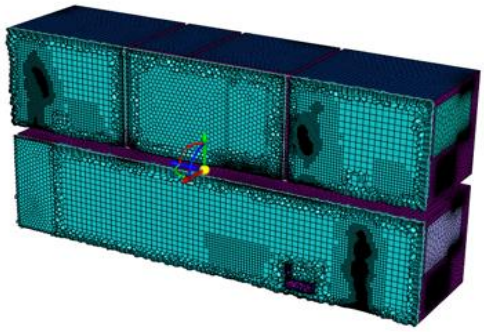

(b)

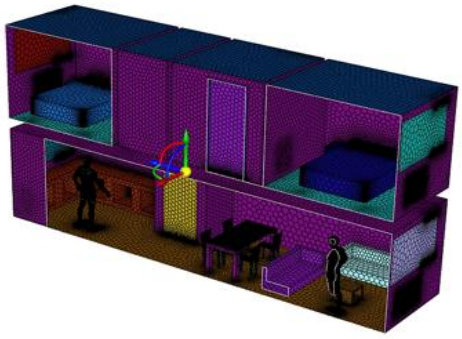

(c)

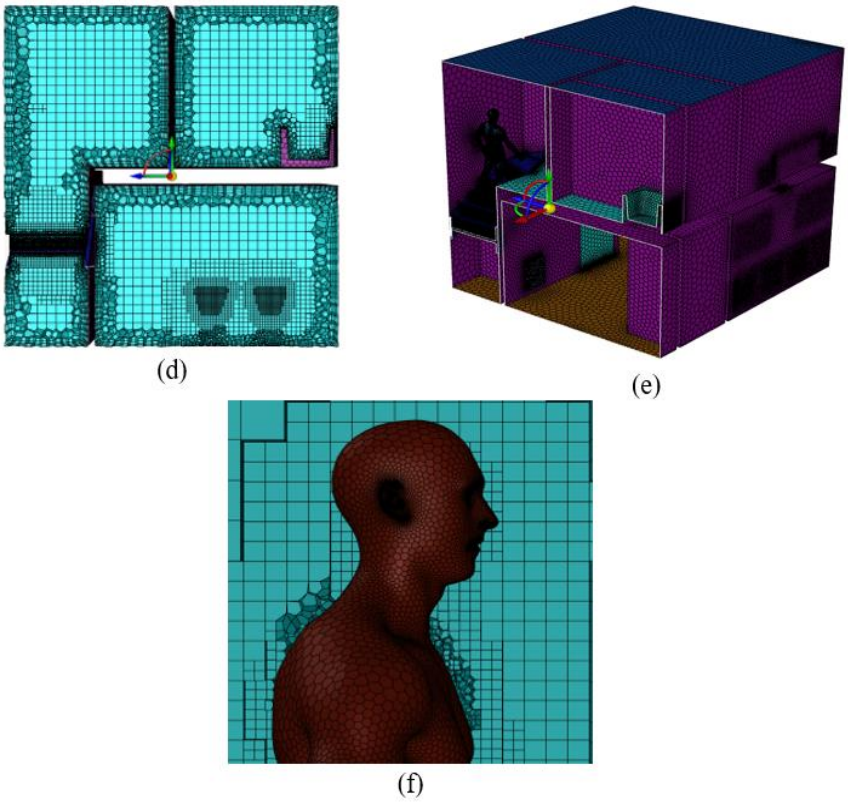

Fig. 3. Computational mesh of the Huddersfield Smart House:
(a) whole-house hybrid poly-hexcore mesh; (b) lengthwise Y-axis mid-section showing the hexahedral core, polyhedral transition and prism layers; (c) full lengthwise Y-axis indoor-domain discretisation; (d) widthwise X-axis mid-section showing local poly-hexcore refinement; (e) full widthwise X-axis indoor-domain discretisation; and (f) mannequin surface mesh with prism inflation layers.

The results in Table 1 show that the medium and fine meshes produced similar predictions for the monitored comfort-related variables. The difference between the medium and fine meshes was approximately 0.41% for temperature and 1.82% for velocity, while the absolute PMV difference was only 0.01. This indicates that further refinement from the production mesh to the fine mesh produced only a small change in the predicted comfort response. The selected production mesh of approximately 4.2 million elements was therefore adopted for the full simulation matrix, as it provided sufficiently stable predictions while maintaining a practical balance between numerical accuracy and computational cost for the twelve transient CFD scenarios.

Because the RNG $k-\varepsilon$ model was used with enhanced wall treatment, the near-wall resolution of the production mesh was also assessed using the non-dimensional wall distance, y^+. The y^+value was calculated as [23][27]:

$$y^+ = \frac{\rho u_\tau y_p}{\mu}$$

where ρ is the air density, u_τ is the friction velocity, y_p is the distance from the wall to

the centroid of the first near-wall cell, and $\mu$is the dynamic viscosity of air. The friction velocity was defined as:

$$u_\tau = \sqrt{\frac{\tau_w}{\rho}}$$

where $\tau_w$is the local wall shear stress.

The y^+ assessment was performed for the adopted production mesh using the same representative summer closed-window 30% RH scenario (S1). Surface groups considered in the assessment included radiator surfaces, window surfaces, mannequin surfaces, floor and internal walls. These regions were selected because they influence radiator plume development, cold-window boundary layers, wall-adjacent velocity gradients and local comfort conditions.

Table 2. Near-wall y^+assessment for the production mesh.

Surface region	Minimum (y^+)	Mean (y^+)	Maximum (y^+)	Interpretation
Radiator surfaces	0.6	1.4	4.2	Adequate near-wall resolution for radiator plume and heat-transfer prediction
Window surfaces	1.1	2.8	6.5	Acceptable resolution of cold-window boundary layers
Mannequin surfaces	0.4	1.2	3.6	Adequate resolution around occupant-level comfort surfaces
Floor	1.4	3.2	8.1	Acceptable near-wall resolution
Internal walls	1.3	3.5	9.0	Acceptable; local higher values remain below 10

The y^+ results in Table 2 show that the production mesh maintained low near-wall distances across the main thermal boundaries, with mean values ranging from 1.2 to 3.5 and maximum values remaining below 10. The radiator and mannequin surfaces, which are particularly important for buoyant plume development and occupant-level comfort extraction, had maximum y^+ values of 4.2 and 3.6, respectively. These results support the suitability of the production mesh for the RNG $k-\varepsilon$ model with enhanced wall treatment and confirm that the near-wall resolution was adequate for the comparative thermal comfort analysis.

Although the y^+ values support the near-wall resolution of the production mesh, they do not remove the inherent turbulence-model limitations of a two-equation RANS closure. The y^+ assessment confirms that the first near-wall cells were placed within an appropriate near-wall range for enhanced wall treatment, but it should not be interpreted as full validation of transitional buoyancy-driven separation or cold-window downdraught dynamics. The mesh and turbulence treatment are therefore considered adequate for comparative scenario-level comfort assessment, while higher-fidelity turbulence modelling would be required for detailed resolution of local downdraught and boundary-layer structures.

The quality of the final mesh was further assessed through cross-sectional inspection

along the two principal building axes. Fig. 3b and Fig. 3c show the lengthwise Y-axis mesh structure, including the poly-hexcore transition, while Fig. 3d and Fig. 3e show the corresponding widthwise X-axis sections. The mannequin surface mesh and prism inflation layers are shown in Fig. 3f.

C. BOUNDARY CONDITIONS AND SIMULATION MATRIX

The radiators were modelled as isothermal surfaces at 60 °C. The external walls were represented as composite constructions with an overall U-value of 0.25 W m^{-2} K^{-1}, while the double-glazed windows were assigned a U-value of 1.8 W m^{-2} K^{-1}. All cases were simulated in transient mode. For the closed-window scenarios, outdoor air entered the building through a lower window slit represented as a velocity inlet and exited through upper slits represented as pressure outlets. For the open-window scenarios, the full window opening was considered open to airflow. In both cases, the inlet velocity was imposed through a custom user-defined function (UDF) based on measured wind-speed time series, thereby generating physically consistent time-varying ventilation conditions. The outdoor temperature and relative humidity values used for each scenario are summarised in Table 3.

Table 3. Complete Simulation Matrix

Season	Scenario ID	Window State	Outdoor Temp. (°C)	Outdoor RH (%)	Clothing (clo)	Metabolic Rate (met)
Summer	S1	Closed	20	30	0.5	1.4
Summer	S2	Open	20	30	0.5	1.4
Summer	S3	Closed	20	50	0.5	1.4
Summer	S4	Open	20	50	0.5	1.4
Summer	S5	Closed	20	70	0.5	1.4
Summer	S6	Open	20	70	0.5	1.4
Winter	W1	Closed	5	30	1.0	1.4
Winter	W2	Open	5	30	1.0	1.4
Winter	W3	Closed	5	50	1.0	1.4
Winter	W4	Open	5	50	1.0	1.4
Winter	W5	Closed	5	70	1.0	1.4
Winter	W6	Open	5	70	1.0	1.4

D. THERMAL COMFORT ASSESSMENT

Thermal comfort was assessed using the Predicted Mean Vote (PMV) and Predicted Percentage of Dissatisfied (PPD) indices in accordance with ISO 7730:2005 [5]. PMV predicts the mean thermal sensation vote of a group of occupants on the standard thermal sensation scale, where negative values indicate cool sensation, positive values indicate warm sensation, and values close to zero indicate thermal neutrality. PPD estimates the percentage of occupants likely to feel thermally dissatisfied under the same conditions. In general, PMV values within approximately −0.5 to +0.5 are commonly interpreted as near-comfort conditions, while larger positive or negative values indicate increasing warm or cool discomfort.

PMV/PPD values were calculated programmatically using the pythermalcomfort Python library (v7.1.0). For each of the 240 extraction points, corresponding to 12 scenarios × 5 mannequin locations × 4 anatomical heights, the required CFD-derived inputs were air temperature, relative humidity, air velocity and mean radiant temperature.

PMV was calculated using Fanger's heat-balance formulation, expressed generally as:

$$PMV = [0.303e^{-0.036M} + 0.028]L$$

where M is the metabolic rate and L is the thermal load on the body, representing the difference between internal heat production and heat loss to the surrounding environment.

PPD was derived directly from PMV using the standard relationship:

$$PPD = 100 - 95e^{-(0.03353PMV^4 + 0.2179PMV^2)}$$

The comfort-category labels reported in Table 3 were assigned based on the PMV/PPD interpretation, where near-zero PMV values indicate thermal neutrality, moderately negative values indicate cool discomfort, and strongly negative values indicate cold discomfort.

In the PMV/PPD calculation, mean radiant temperature (T_r) was approximated using the local air temperature (T_a) extracted from the CFD field:

$$T_r(\mathrm{x}) \approx T_a(\mathrm{x})$$

This approximation was adopted because the CFD simulations did not include an explicit radiation model and therefore did not produce spatially resolved incident radiation fields from which local mean radiant temperature could be calculated. Under this assumption, the PMV calculation primarily reflects the combined effects of local air temperature, air velocity, relative humidity, clothing insulation and metabolic rate, but it does not fully resolve local radiant asymmetry.

This treatment is acceptable for a comparative assessment of scenario-level comfort trends, particularly where the objective is to examine the relative influence of season, window state and humidity. However, it is a simplification in a radiator-heated environment because the model includes warm radiator surfaces and cold window boundary conditions. Local radiant discomfort near cold glazing or close to heated radiator panels may therefore be underestimated. The PMV/PPD results should consequently be interpreted as comparative air-temperature-based comfort indicators rather than as full radiant-comfort predictions.

The personal parameters were kept constant within each season. Metabolic rate was set to 1.4 met to represent light standing domestic activity, external work was set to 0 met, clothing insulation was set to 0.5 clo for summer scenarios and 1.0 clo for winter scenarios. These values were selected to represent light domestic activity and seasonally appropriate clothing conditions. They also provide a consistent basis for comparing the twelve scenarios, since variations in metabolic rate and clothing insulation can strongly influence PMV/PPD predictions [18][19].

The m3-ankle point consistently showed anomalously high temperatures due to its location within the stairs/landing region. This point was therefore excluded from zonal-average comfort summaries to avoid biasing the mean values for the main occupied zones. However, it was retained in the spatial interpretation because it represents a physically meaningful local thermal anomaly associated with buoyancy-driven air movement and heat accumulation within the stairwell zone.

E. STATISTICAL ANALYSIS OF THERMAL COMFORT PARAMETERS

A descriptive statistical analysis was performed on the 240 comfort observations and their corresponding environmental variables, including air temperature, relative humidity and air velocity. The purpose of the statistical analysis was to identify dominant trends in the CFD-derived comfort dataset rather than to establish independent causal relationships. Summary statistics, including mean, standard deviation, minimum and maximum values, were calculated for PMV, PPD, air temperature, relative humidity and air velocity. Simple linear regression models of the form

$$y = \beta_0 + \beta_1 x$$

were fitted to examine pairwise associations between the environmental variables and the comfort indices. The coefficient of determination (R^2) was used only as a descriptive measure of the strength of linear association within the simulated dataset. Because the extracted observations are nested within scenarios, mannequin locations and anatomical heights, the regression results were not interpreted as fully independent inferential statistics.

The PMV-PPD relationship was not treated as an independent empirical regression because PPD is analytically derived from PMV using the standard ISO/Fanger relationship. Any PMV-PPD plot was therefore used only as a consistency check and visual confirmation of the standard transformation from thermal sensation to predicted dissatisfaction. Similarly, the strong PMV-air-temperature association was interpreted with caution because local air temperature was also used as the proxy for mean radiant temperature in the PMV calculation. The statistical outputs should therefore be understood as descriptive indicators of comfort-pattern sensitivity within the present modelling assumptions.

F. BASIS FOR COMFORT METRIC EXTRACTION

Although all cases were simulated in transient mode using time-varying inlet forcing derived from measured wind-speed data, the comfort metrics reported in this study were extracted from the final simulated time step of each scenario. This approach was adopted to provide a consistent terminal-response basis for comparison across the twelve cases. The study should therefore be interpreted as a scenario-end-state comfort assessment rather than a full-time history analysis of transient comfort fluctuations. This distinction is important because the present conclusions concern comparative scenario performance, not short-term temporal variability such as intermittent draught peaks.

G. VALIDATION PROCEDURE

The CFD framework was compared with experimental microclimate measurements obtained under matched indoor conditions to provide point-based validation of selected occupant-relevant comfort variables. The validation was based on discrete measurements at body-height locations and was not intended to confirm the full three-dimensional transient temperature, velocity or humidity fields. Therefore, the airflow and temperature contours reported in this study should be interpreted as CFD-predicted spatial fields rather than experimentally measured full-domain fields.

The first living-room validation setup is shown in Fig. 4. A body-height reference pole was positioned in the living room area to represent the CFD mannequin extraction heights, namely forehead level at 1.62 m, chest level at 1.30 m, knee level at 0.42 m and ankle level at 0.07 m. Thermocouple wires were fixed at each of these levels to record local air temperature, with data logged

through a PicoLog system and retrieved using PicoLog software on a laptop.

A DeltaOhm HD32.3TC microclimate comfort sensor was positioned close to the reference pole to measure the main comfort-related environmental parameters, including air speed and relative humidity, required for PMV/PPD calculation. This arrangement allowed measured indoor microclimate conditions to be compared with simulated values extracted at corresponding occupant-relevant heights. Validation was performed for two closed-window summer scenarios, S1 and S3, at mannequin locations m1 and m2, representing the living room and kitchen areas.

Direct experimental comparison was limited to the closed-window summer scenarios because these were the cases for which matched PMV and PPD measurements were available under the most stable and controllable indoor conditions. The open-window and winter scenarios involve stronger infiltration, greater thermal stratification and more complex transient behaviour, but equivalent experimental datasets were not available for the present study. Therefore, these cases are interpreted as comparative CFD predictions within an experimentally supported modelling framework, rather than as fully experimentally verified spatial fields.

As shown in Figs. 5 and 6, the agreement between simulation and experiment was good for Scenario S1, with PMV deviations of about 0.08 at both locations and an average PPD deviation of about 2.71 percentage points. For Scenario S3, the PMV deviation again remained about 0.08, while the average PPD deviation was about 2.57 percentage points. Across both scenarios, the CFD framework slightly underestimated PPD but remained close to the measured values overall.

These results support the use of the model for comparative comfort assessment under the measured closed-window summer conditions. However, because the validation was based on discrete point measurements, the results should not be interpreted as full-field experimental validation of the predicted spatial thermal heterogeneity. The lack of direct experimental validation for winter, open-window and full-domain spatial fields remains a limitation and is explicitly considered in the interpretation of the results.

10.37965/jdmd.2026.1308

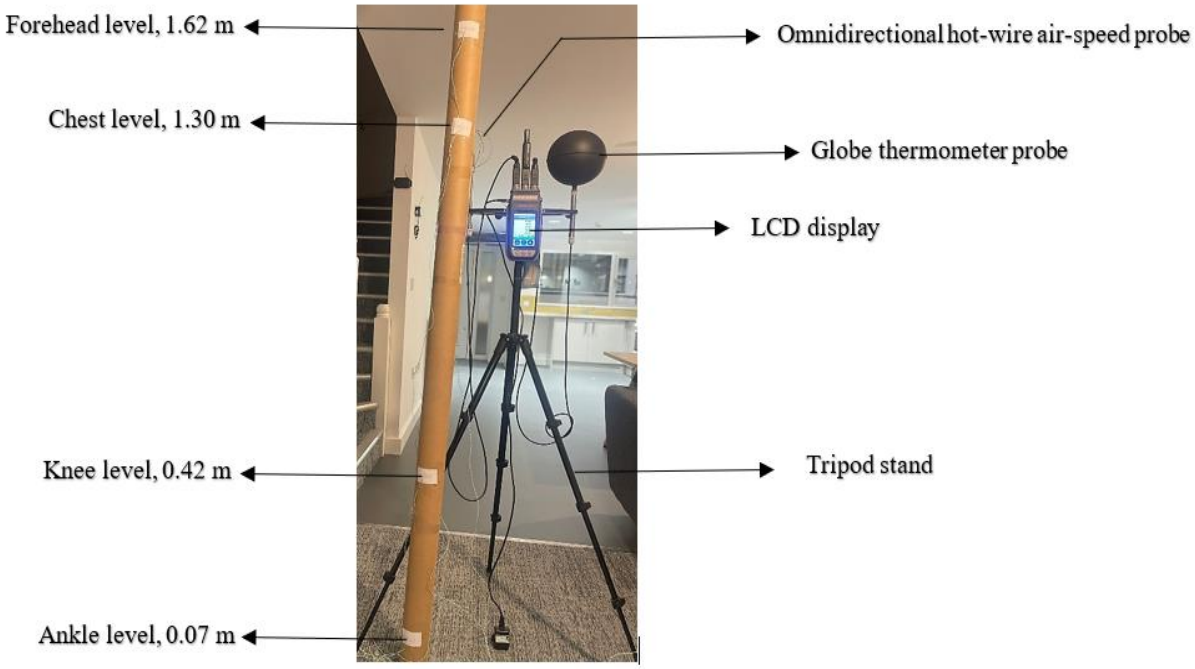

Fig. 4. Living room experimental validation setup showing the body-height reference pole and DeltaOhm HD32.3TC microclimate comfort sensor used for CFD thermal comfort validation.

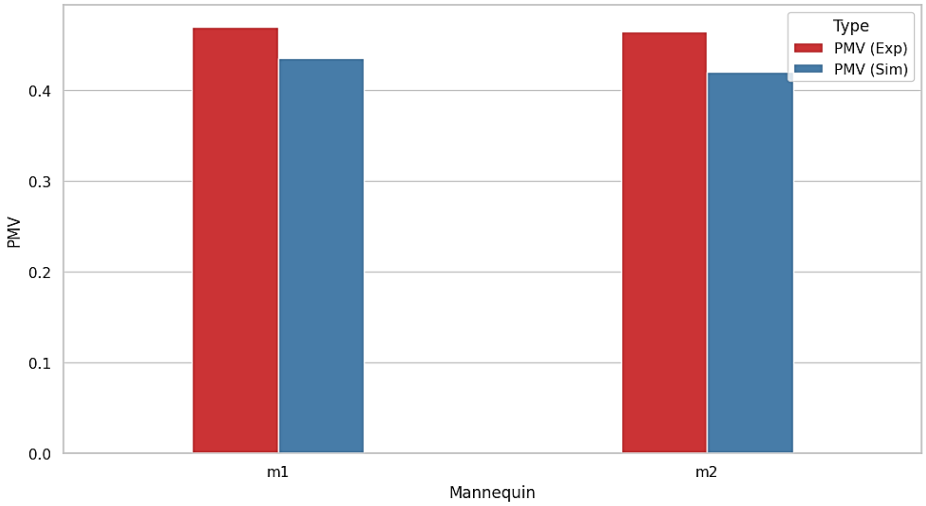

Fig. 5. PMV - Experimental vs Simulated Results for scenario 1 and 3

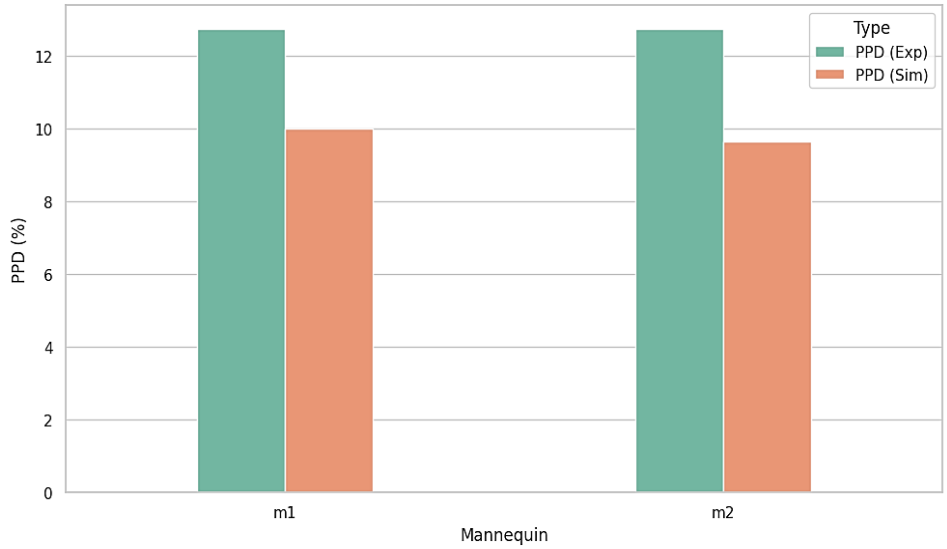

Fig. 6. PPD - Experimental vs Simulated Results for scenario 1 and 3

III. RESULTS

A. THERMAL COMFORT OUTCOMES

Table 4 summarises the average PMV and PPD outcomes for all twelve scenarios using a metabolic rate of 1.4 met and seasonal clothing levels. Clear scenario-dependent patterns are observed. In the summer closed-window cases (S1, S3 and S5), the indoor environment remained slightly warm, with average PMV values between 0.45 and 0.58 and average PPD values between 12.1% and 15.3%. These results indicate conditions close to, but not fully within, common comfort acceptability targets. In the summer open-window cases (S2, S4 and S6), the additional ventilation caused marked cooling, shifting the average PMV to between −1.21 and -1.34 and increasing average PPD to 38.7-43.2%. In winter, the radiator system was unable to maintain acceptable comfort even with windows closed: average PMV ranged from -1.52 to -1.63 and average PPD from 52.8% to 57.1%. Winter open-window cases represented the most severe conditions, with average PMV between -2.18 and -2.24 and average PPD above 82%. The m3-ankle point remained a persistent local anomaly due to its elevated local temperature relative to the surrounding occupied zone and is therefore treated separately from zonal-average interpretation.

Table 4. Summary of Thermal Comfort Indices (PMV/PPD)

Scenario	Season	Window State	RH (%)	Avg. PMV	Avg. PPD (%)	Comfort Category
S1	Summer	Closed	30	0.45	12.1	Slightly Warm
S2	Summer	Open	30	-1.28	41.5	Cool
S3	Summer	Closed	50	0.52	13.8	Slightly Warm
S4	Summer	Open	50	-1.34	43.2	Cool
S5	Summer	Closed	70	0.58	15.3	Slightly Warm

S6	Summer	Open	70	-1.21	38.7	Cool
W1	Winter	Closed	30	-1.52	52.8	Cool
W2	Winter	Open	30	-2.18	82.1	Cold
W3	Winter	Closed	50	-1.58	55.3	Cool
W4	Winter	Open	50	-2.24	84.6	Cold
W5	Winter	Closed	70	-1.63	57.1	Cool
W6	Winter	Open	70	-2.19	83.2	Cold

B. SPATIAL ANALYSIS OF AIRFLOW AND TEMPERATURE DISTRIBUTION

The CFD simulations produced high-resolution predicted airflow and temperature fields for all twelve scenarios and indicated substantial spatial non-uniformity across the house. These spatial fields should be interpreted as CFD-predicted distributions rather than experimentally measured full-domain fields, because full-field optical validation or high-density sensor-based mapping was not performed in the present study.

The following sections describe the principal predicted flow and temperature patterns shown in Figs. 7-14, with emphasis on vertical stratification, ventilation-driven cooling and the persistent stair/landing anomaly. To support direct visual comparison between scenarios, consistent legend ranges were used within each comparable group of velocity and temperature plots. Rather than relying only on scenario-average PMV/PPD values, the spatial analysis demonstrates how local predicted thermal conditions vary across rooms, mannequin locations and body heights.

1. CLOSED-WINDOW SCENARIOS

In the summer closed-window scenarios (S1, S3 and S5), the velocity contours in Fig.7 show generally low indoor air movement across the occupied zones. Most mannequin planes are dominated by blue to cyan regions on the unified velocity scale, indicating low air speeds, typically below about 0.2-0.3 m/s, with only localised higher-velocity regions close to openings, edges or recirculation paths. This confirms that the closed-window cases were characterised by weak indoor airflow and limited mixing.

The temperature contours in Fig. 8 show a relatively stable but stratified thermal field. The unified temperature legend includes the hot radiator surface range; therefore, the occupied-zone air temperatures appear mainly within the green-to-yellow region rather than the upper red range. Quantitative point extractions showed that head-level temperatures were approximately 26.7-28.4 °C, while ankle-level temperatures were approximately 25.3-26.1 °C, giving a vertical temperature difference of about 2-3 °C across the mannequin heights. These results indicate a slightly warm and vertically stratified indoor condition, consistent with the average PMV range of 0.45-0.58.

A local anomaly was also identified at the m3-ankle position near the stair/landing region, where the extracted temperature reached about 30 °C. This point was warmer than the surrounding occupied-zone locations and produced a locally elevated PMV of about 1.27. Because this behaviour was associated with a specific transitional zone, it was treated separately from the general zonal-average comfort interpretation.

30% RH 50% RH 70% RH

10.37965/jdmd.2026.1308

Whole-domain Velocity volume rendering

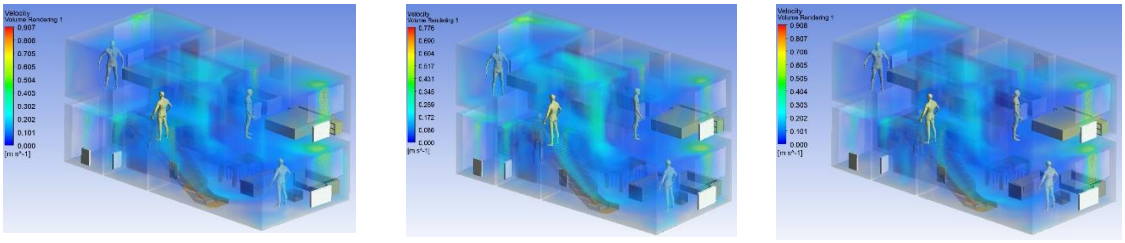

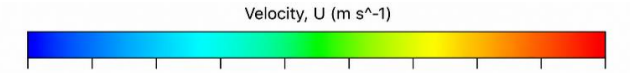

Velocity plane m1

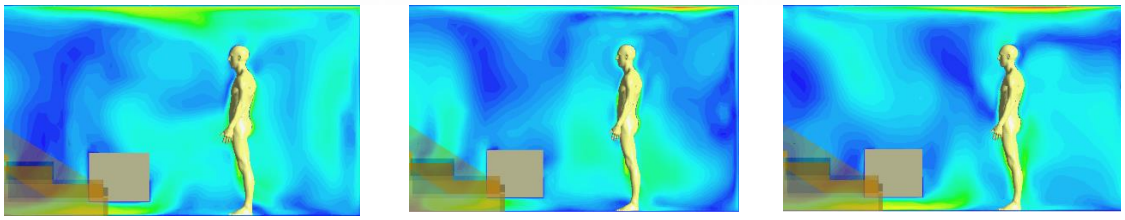

Velocity plane m2

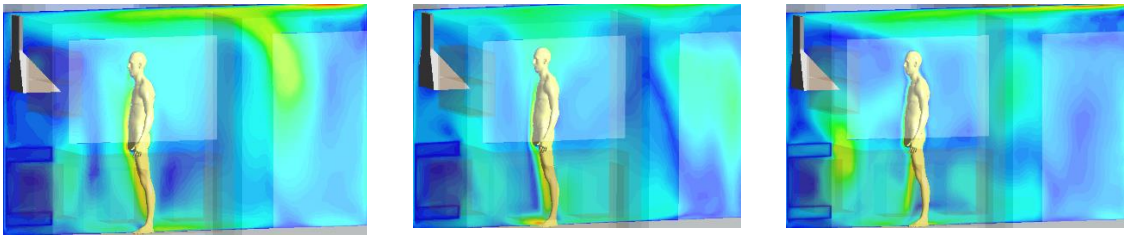

Velocity plane m3

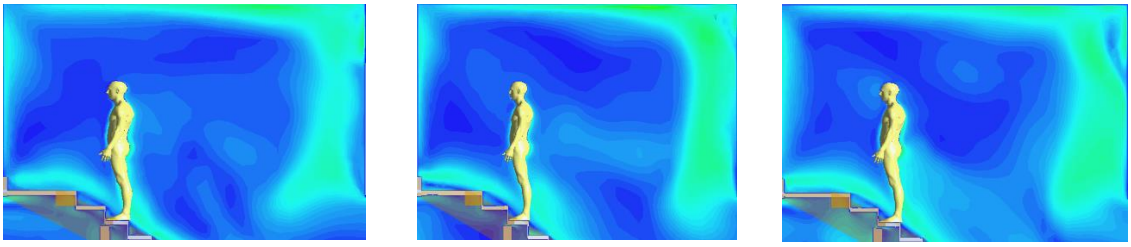

Velocity plane m4

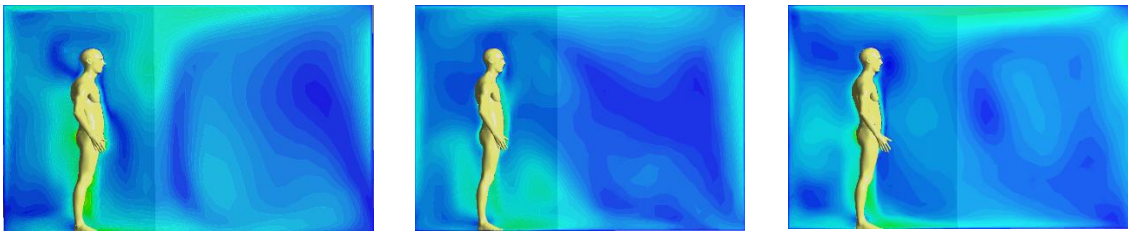

Velocity plane m5

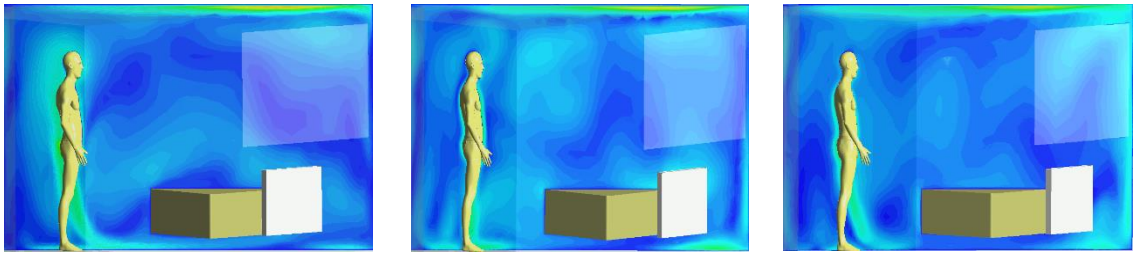

10.37965/jdmd.2026.1308

Fig 7. Air velocity distribution at mannequin planes for summer closed-window scenarios (outdoor temperature: 20°C). Columns show results for 30%, 50%, and 70% relative humidity. A unified velocity legend is used to support comparison across the 30%, 50% and 70% RH cases.

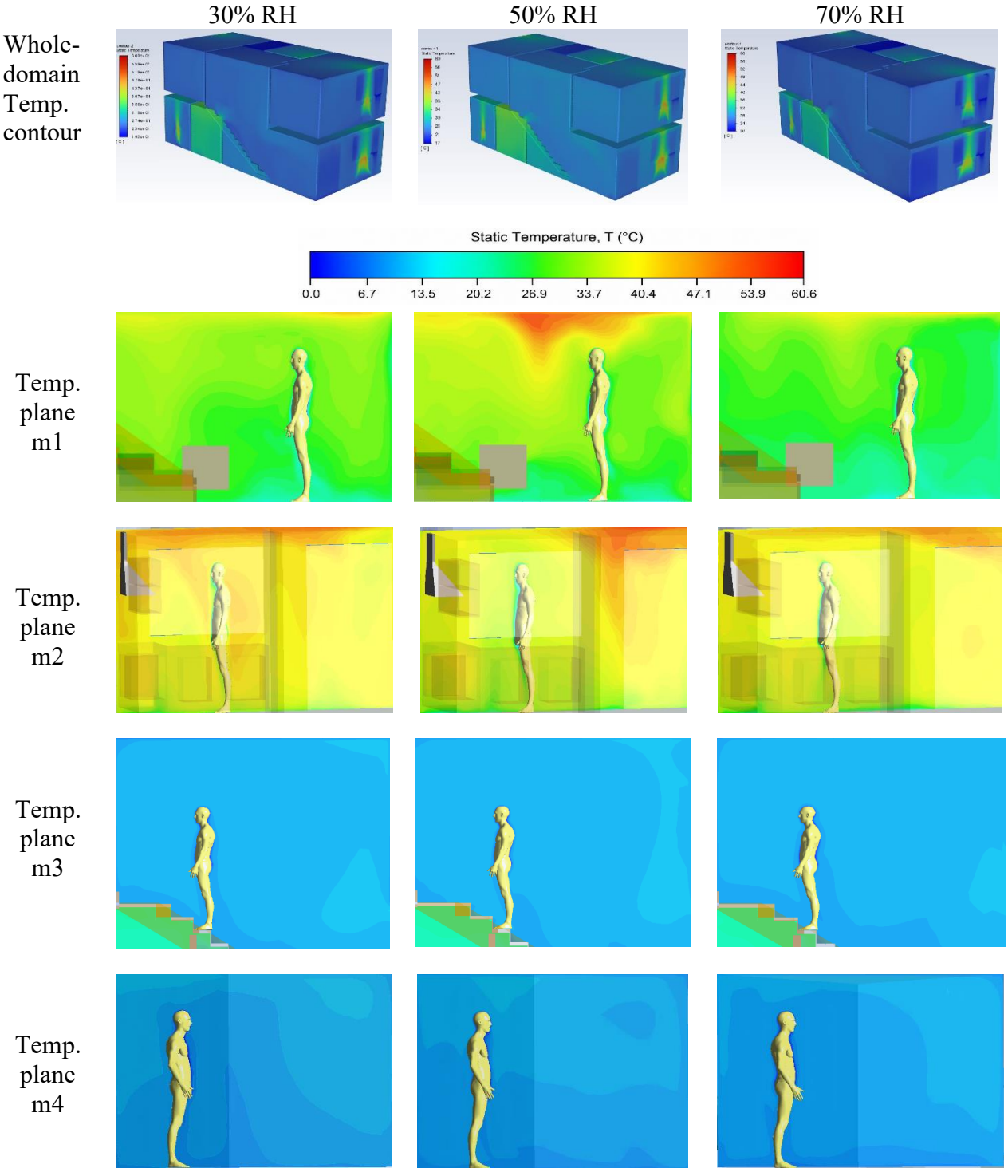

10.37965/jdmd.2026.1308

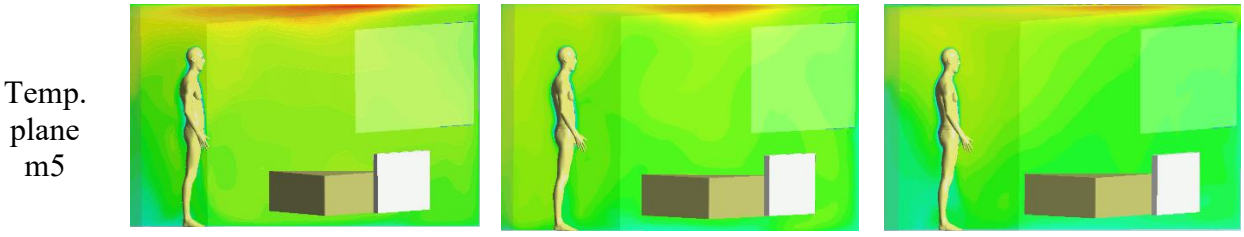

Fig 8. Temperature distribution at mannequin planes for summer closed-window scenarios (outdoor temperature: 20 °C). Columns show results for 30%, 50%, and 70% relative humidity. A unified temperature legend is used; the upper range includes radiator and hot-surface temperatures, while occupied-zone air temperatures are interpreted using extracted mannequin-plane values.

Winter Conditions (Figs. 9 and 10).

Under winter closed-window operation (W1, W3 and W5), the velocity contours in Fig. 9 show generally low indoor air movement across the mannequin planes. Most regions remain within the blue-to-cyan range on the unified velocity scale, indicating weak airflow, typically below about 0.3 m/s, with only localised higher-velocity regions near openings, edges or recirculation paths. This suggests that, despite closed-window operation, indoor mixing remained limited.

The temperature contours in Fig. 10 show a non-uniform thermal field, with warmer regions close to radiator-influenced surfaces and cooler conditions across several occupied-zone planes. Because the unified temperature legend includes the hot radiator/surface range, the comfort interpretation was supported by quantitative mannequin-point extractions rather than colour contours alone. These extracted values showed that several occupied-zone temperatures remained low, approximately 13-16 °C, which was below typical comfort conditions. This produced cool-discomfort PMV values of about -1.43 to -1.98 in the main occupied zones.

The m3-ankle anomaly was again observed near the stair/landing region, where extracted temperatures remained comparatively higher, approximately 23.8-25.3 °C. This localised warm region produced a PMV value up to about 3 points higher than adjacent cooler zones. The result indicates a clear zonal imbalance and weak thermal mixing, rather than uniform whole-house comfort under winter closed-window conditions.

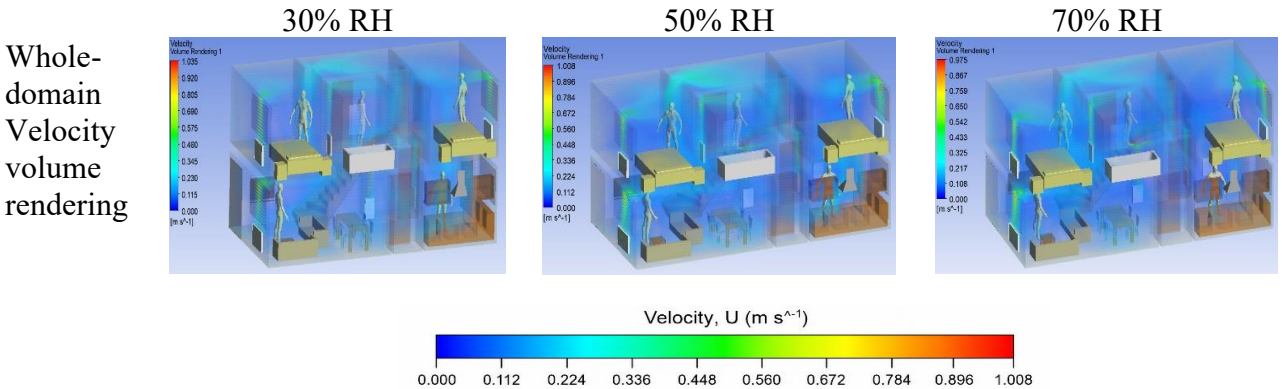

10.37965/jdmd.2026.1308

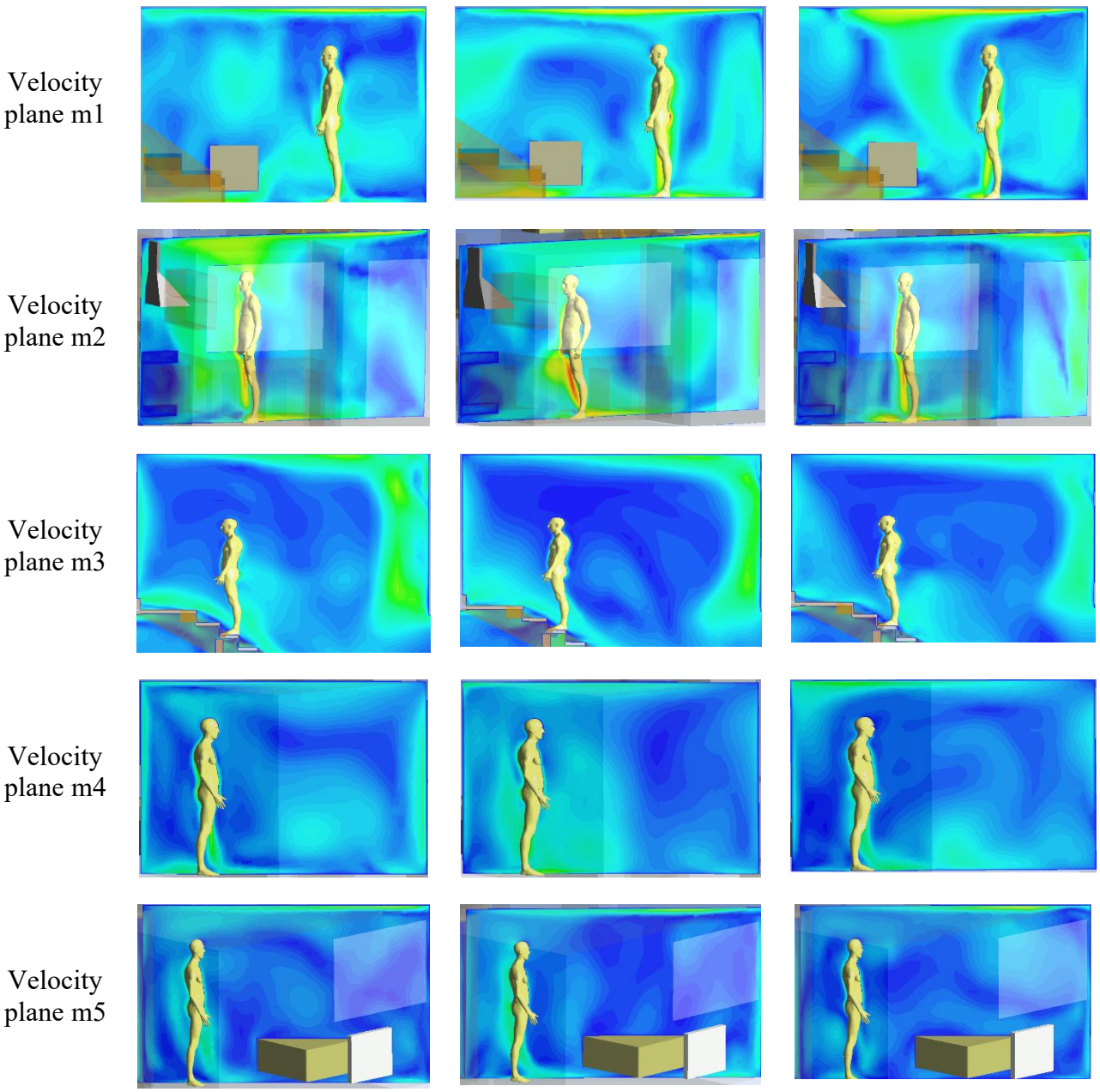

Fig 9. Air velocity distribution at mannequin planes for winter closed-window scenarios (outdoor temperature: 5°C). Columns show results for 30%, 50%, and 70% relative humidity. A unified velocity legend is used to support comparison across the 30%, 50% and 70% RH cases.

10.37965/jdmd.2026.1308

Whole-domain Temp. contour

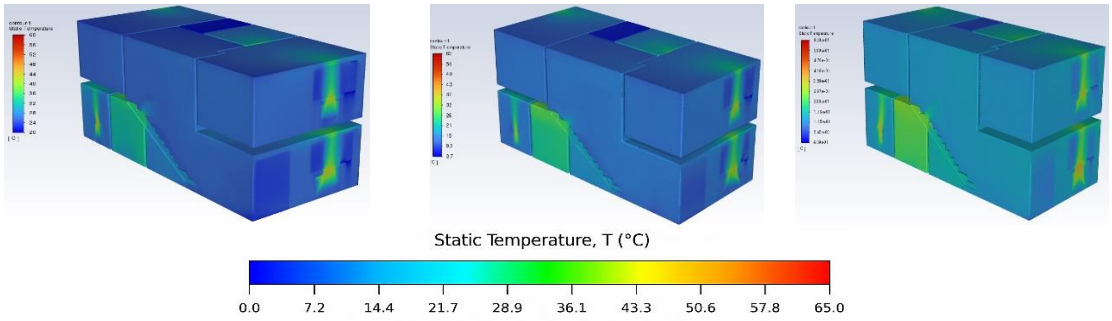

Temp. plane m1

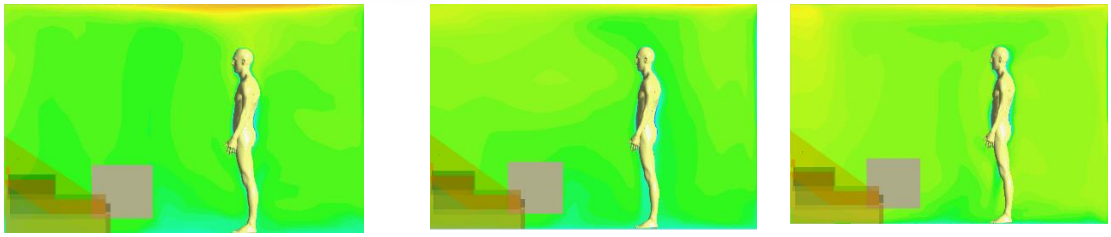

Temp. plane m2

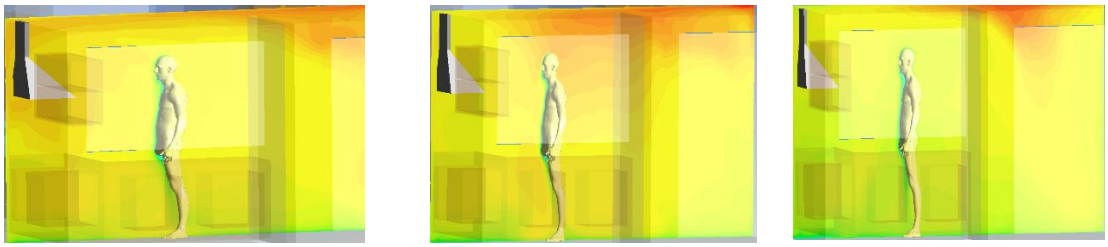

Temp. plane m3

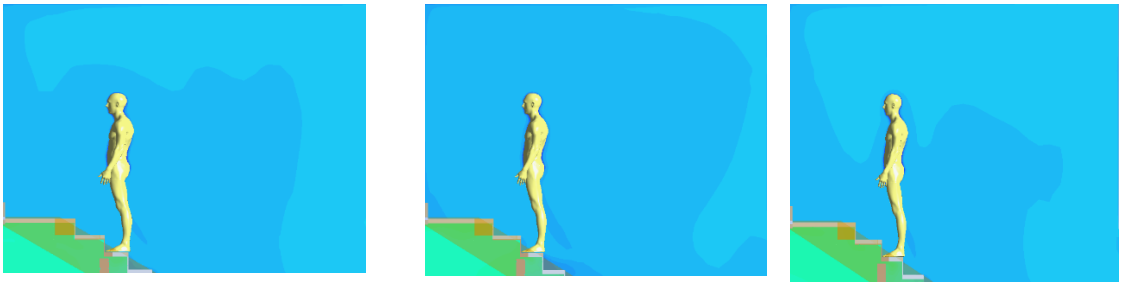

Temp. plane m4

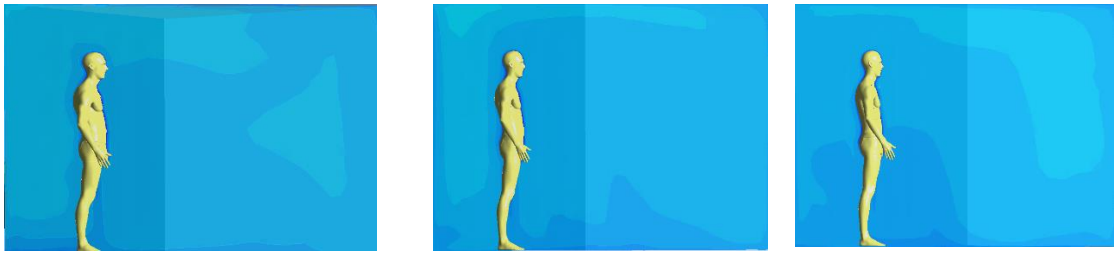

10.37965/jdmd.2026.1308

Temp. plane m5

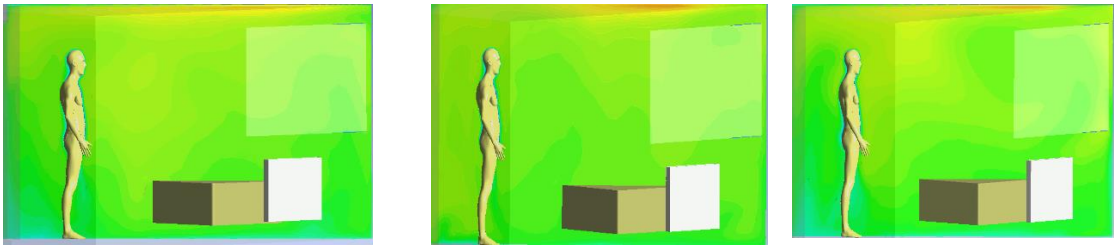

Fig 10. Temperature distribution at mannequin planes for winter closed-window scenarios (outdoor temperature: 5°C). Columns show results for 30%, 50%, and 70% relative humidity. A unified temperature legend is used; the upper range includes radiator and hot-surface temperatures, while occupied-zone comfort interpretation is based on extracted mannequin-plane values.

2. OPEN-WINDOW SCENARIOS

Summer Conditions (Figs. 11 and 12).

Opening the windows produced a clear change in the summer airflow pattern (S2, S4 and S6). Compared with the closed-window cases, the velocity planes in Fig. 11 show stronger air movement and more visible flow variation around the mannequin locations. Although the unified velocity legend extends to higher local values, the occupied-zone extractions showed air speeds of up to about 0.55 m/s, with the highest values occurring around the stairwell region, particularly near m3-knee. This indicates that window opening increased ventilation-driven airflow and reduced the stability of the indoor thermal field.

The temperature contours in Fig. 12 show a cooler occupied-zone environment than the summer closed-window cases. Since the unified temperature legend includes both low boundary values and hot-surface effects, the comfort interpretation was supported by quantitative point extractions. These showed that most occupied-zone temperatures reduced to approximately 20-23 °C, indicating substantial cooling due to ventilation heat loss. The combined effect of lower air temperature and increased air velocity shifted the PMV values into the cool-discomfort range, approximately -0.84 to -1.78.

The m3-ankle position remained a local outlier, with extracted temperatures still reaching approximately 25-30 °C in some cases. This produced locally warmer PMV values within an otherwise cooler indoor environment, confirming that the stair/landing region behaved differently from the main occupied zones and should be interpreted separately from the overall zonal comfort response.

30% RH 50% RH 70% RH

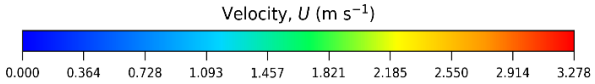

10.37965/jdmd.2026.1308

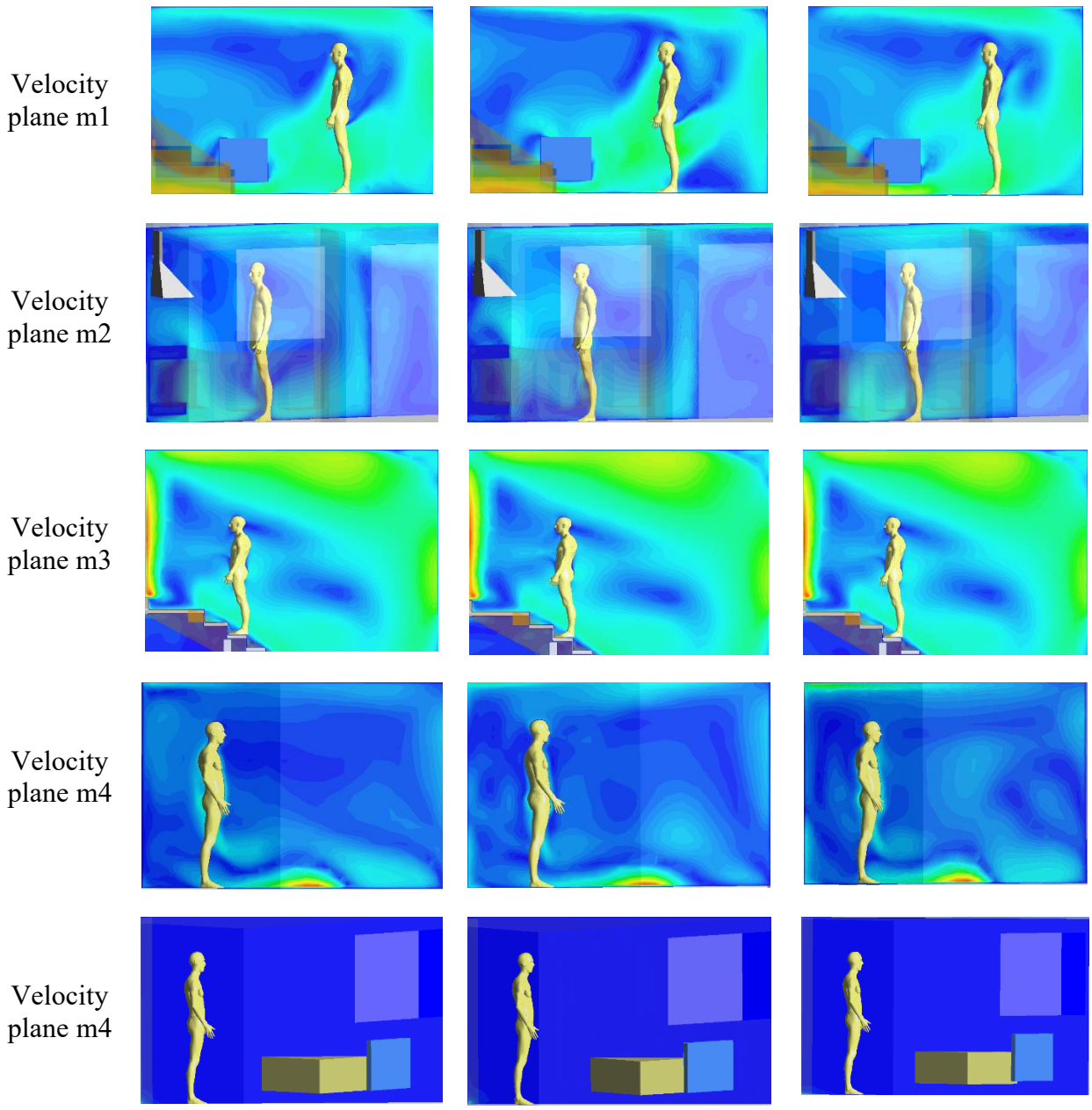

Fig 11. Air velocity distribution at mannequin planes for summer open-window scenarios (outdoor temperature: 20°C). Columns show results for 30%, 50%, and 70% relative humidity. A unified velocity legend is used; occupied-zone interpretation is based on extracted mannequin-plane values to avoid over-reliance on colour variation alone.

10.37965/jdmd.2026.1308

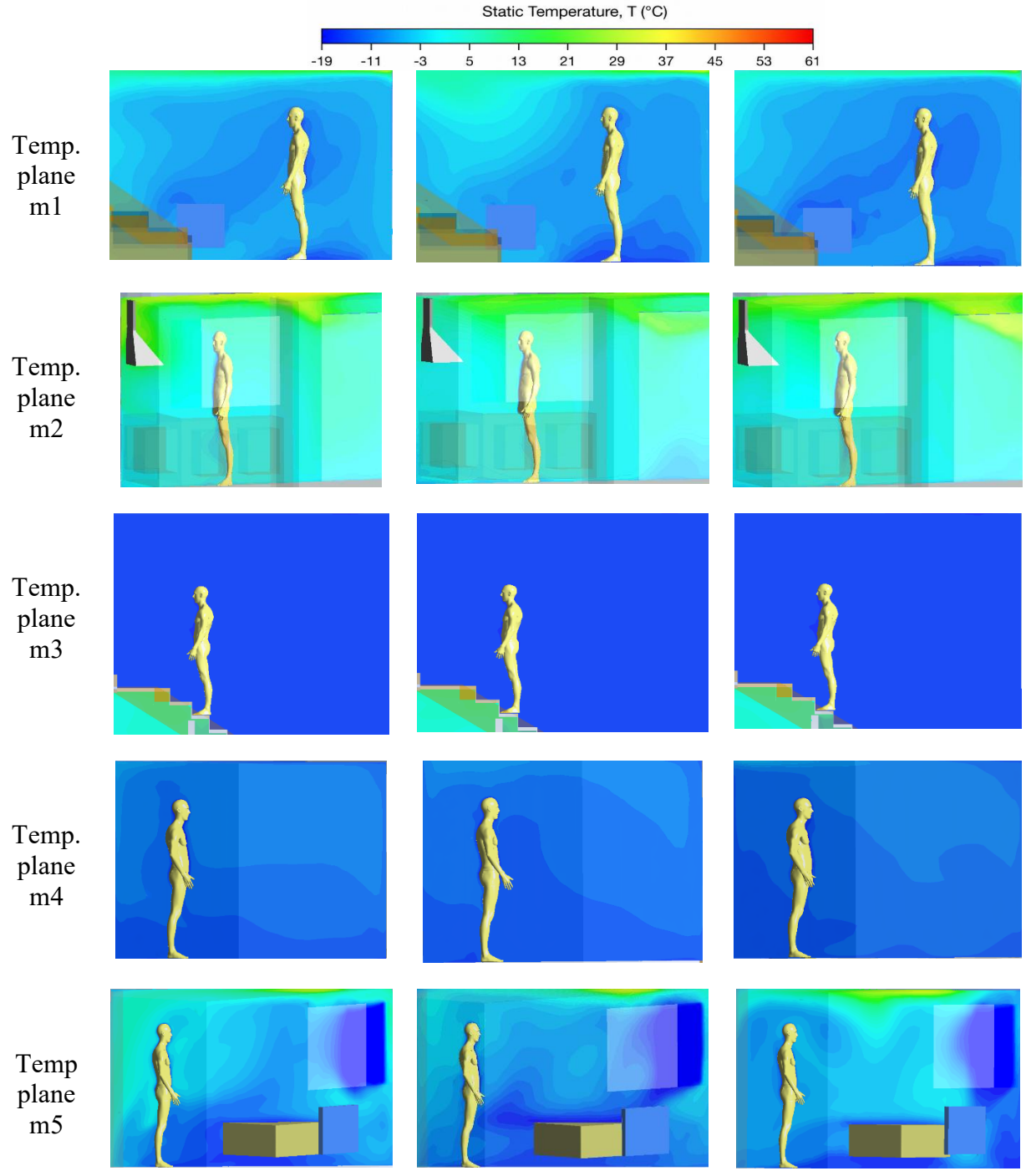

Fig 12. Temperature distribution at mannequin planes for summer open-window scenarios (outdoor temperature: 20°C). Columns show results for 30%, 50%, and 70% relative humidity. A unified temperature legend is used; the wide range includes boundary and hot-surface effects, while comfort interpretation is based on extracted occupied-zone values.

The winter open-window scenarios (W2, W4 and W6) produced the most severe thermal conditions. The velocity contours in Fig. 13 show stronger airflow variation than the closed-window winter cases, with increased movement around the stairwell and window-influenced zones. Although the unified velocity legend extends to high local values, the occupied-zone extractions showed air speeds reaching approximately 0.57 m/s in selected regions, indicating increased cold-air infiltration and ventilation-driven flow.

The temperature contours in Fig. 14 show clear cooling across most occupied-zone planes. Because the unified temperature legend includes both low boundary values and hot-surface effects, the comfort interpretation was supported by extracted mannequin-point values. These showed that several occupied-zone temperatures fell to approximately 6-12 °C, confirming substantial temperature depression under winter open-window operation. As a result, PMV values shifted into severe cold-discomfort conditions, ranging from approximately -2.08 to -3.70, with corresponding PPD values above 80-99%.

Despite the generally cold indoor environment, the m3-ankle point remained a local thermal anomaly, with extracted temperatures of approximately 21.9-25.4 °C. This indicates that the stair/landing region retained a comparatively warmer local condition than the surrounding occupied zones. The result highlights poor zonal balance and limited thermal mixing in this isolated area, rather than uniform whole-house comfort.

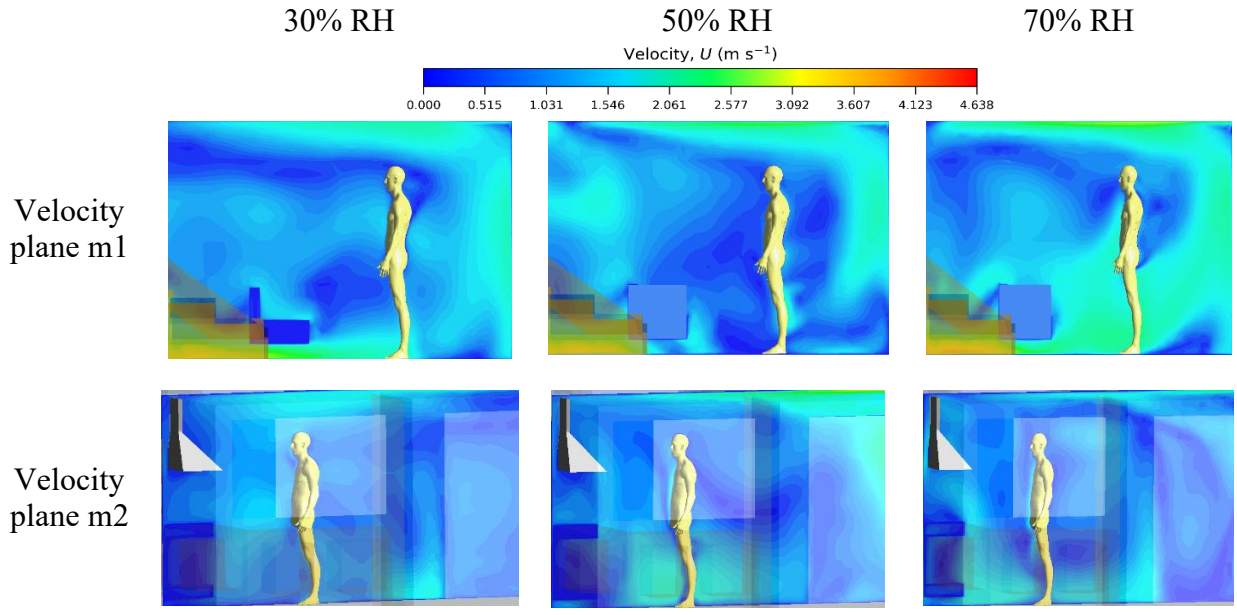

10.37965/jdmd.2026.1308

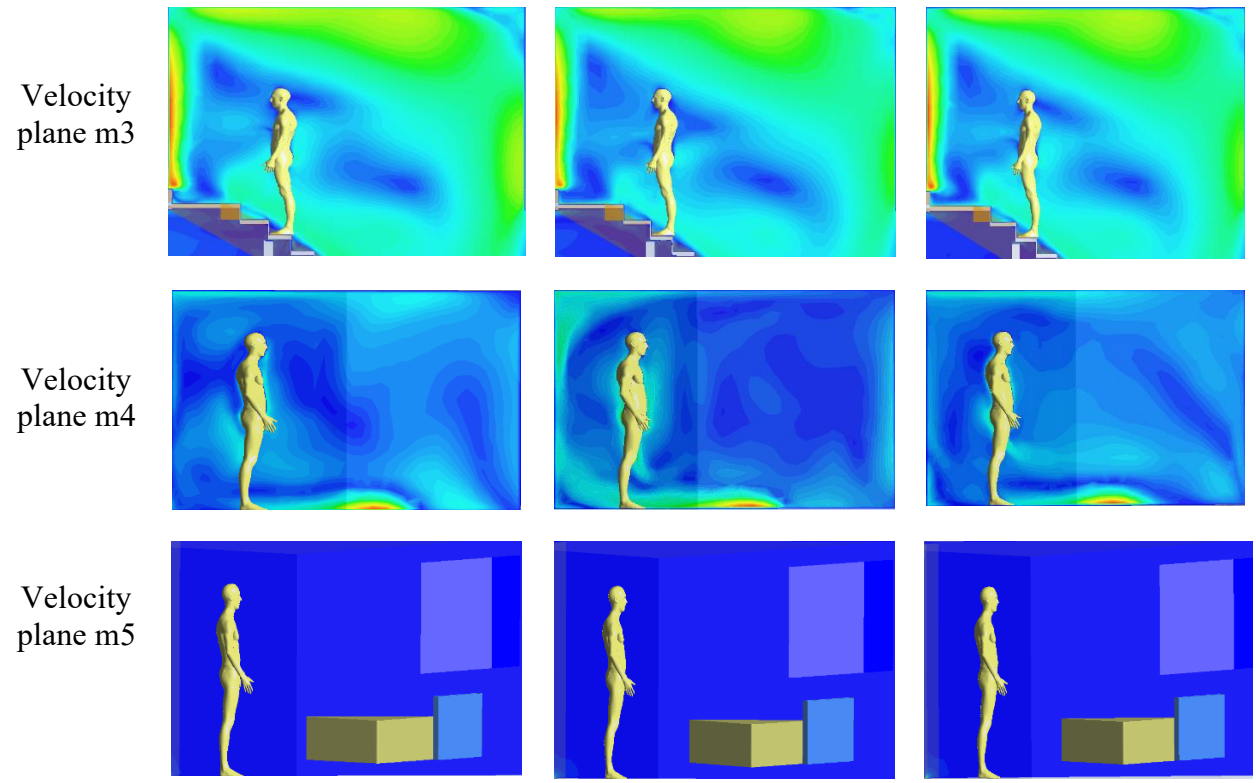

Fig 13. Air velocity distribution at mannequin planes for winter open-window scenarios (outdoor temperature: 5°C). Columns show results for 30%, 50%, and 70% relative humidity. A unified velocity legend is used; occupied-zone interpretation is based on extracted mannequin-plane values because local boundary regions may produce higher velocities than the main occupied zones.

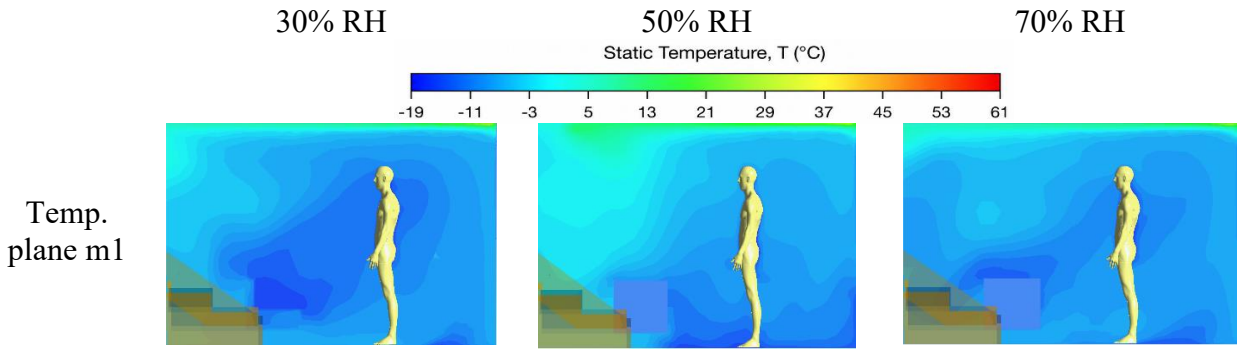

10.37965/jdmd.2026.1308

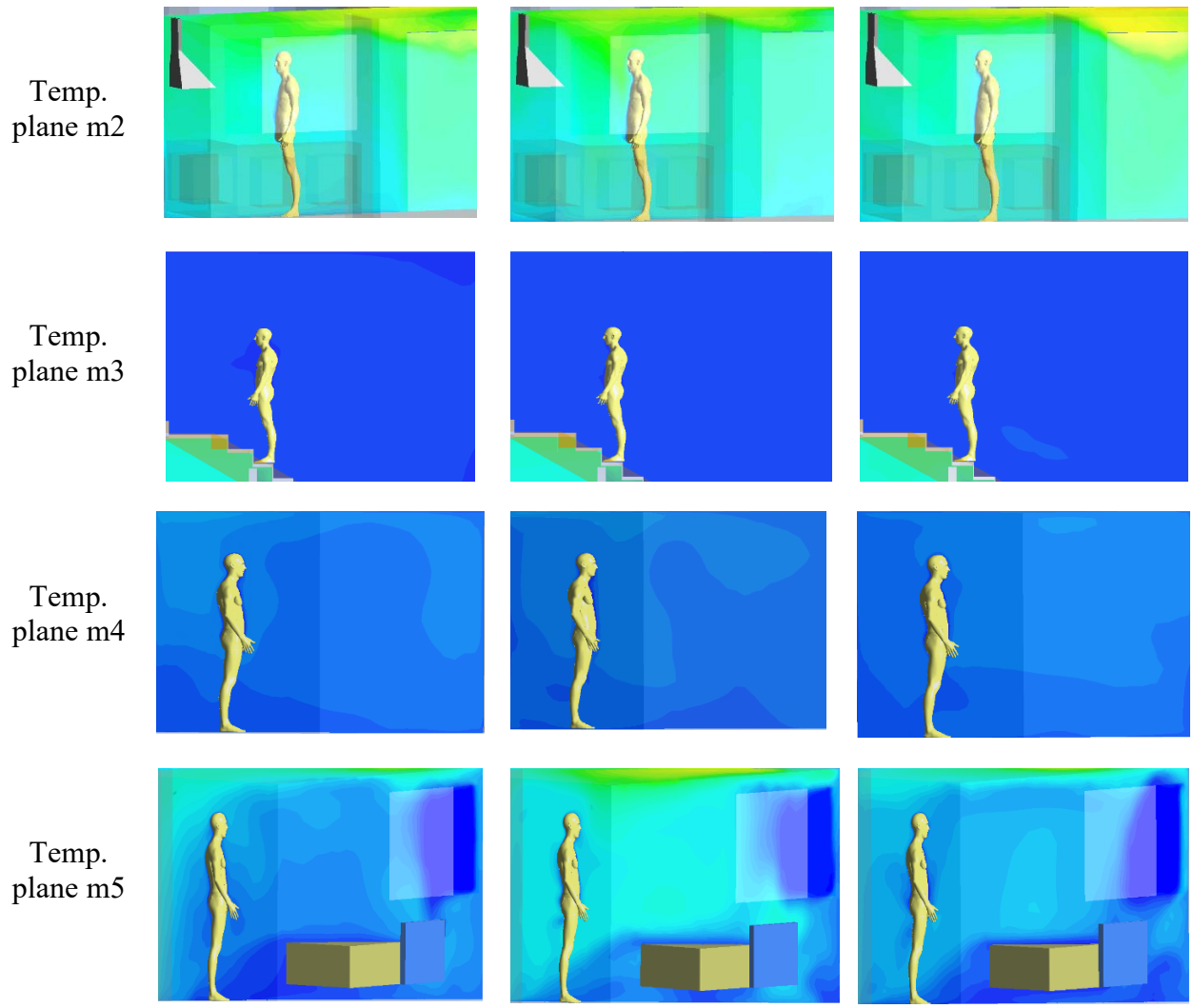

Fig 14. Temperature distribution at mannequin planes for winter open-window scenarios (outdoor temperature: 5°C). Columns show results for 30%, 50%, and 70% relative humidity. A unified temperature legend is used; the wide range includes boundary and hot-surface effects, while comfort interpretation is based on extracted occupied-zone values.

C. STATISTICAL COMFORT DISTRIBUTION

Table 5 summarises the central tendency and variability of the PMV/PPD data across the four grouped scenario classes. Closed-window scenarios showed lower PMV variability, consistent with more stable and stratified indoor conditions, whereas open-window scenarios showed higher variability due to the stronger and more heterogeneous airflow introduced by ventilation. The highest mean PPD occurred in the winter open-window cases, confirming the severe discomfort already observed in the temperature fields. Because the m3-ankle point reflects a recurring local anomaly, the

grouped statistics should be interpreted alongside the spatial results rather than in isolation.

Table 5. Statistical Summary of Thermal Comfort Indices.

Statistic	Summer Closed PMV	Summer Open PMV	Winter Closed PMV	Winter Open PMV
Mean	0.48	-1.26	-1.57	-2.45
Standard Deviation	0.23	0.35	0.28	0.52
Minimum	-0.16	-2.01	-2.20	-3.70
Maximum	1.33	1.19	0.73	0.63
PPD Mean (%)	**14.3**	**41.8**	**55.7**	**85.2**

D. REGRESSION OUTPUT

The regression analysis indicates that air temperature was the strongest environmental predictor of PMV and PPD within the present dataset. PMV increased strongly with air temperature, while PPD decreased as air temperature increased. This trend is physically consistent with the wide temperature spread across the simulated scenarios. However, the strength of this relationship should be interpreted in the context of the modelling approach, because mean radiant temperature was approximated using local air temperature in the PMV calculation. Therefore, the high (R^2) value for PMV versus air temperature reflects both the physical influence of air temperature and the structure of the PMV input assumptions.

Relative humidity and air velocity showed much weaker linear relationships with PMV and PPD. This indicates that, within the tested range, humidity and air speed acted as secondary modifiers compared with the dominant effect of temperature and window state. The PMV-PPD relationship was not interpreted as an independent statistical finding because PPD is calculated directly from PMV using the standard analytical relationship. It is therefore reported only as a consistency check rather than as evidence of an empirical correlation.

Overall, the regression analysis as shown in Table 6 and 7, supports the descriptive interpretation that air temperature and window state dominate the comfort response in the present scenario set, while relative humidity and air velocity have smaller linear effects under the tested conditions.

Table 6. Descriptive linear regression results between environmental predictors and comfort indices ($n = 240$).

Relationship	R^2	Slope	Intercept	p-value	n
PMV vs Temperature	0.9246	0.1791	-4.5659	1.28e-135	240

Relationship	R^2	Slope	Intercept	p-value	n
PMV vs RH	0.0233	-0.0135	-0.7881	0.0180	240
PMV vs Air Velocity	0.0744	-3.5689	-0.8473	1.84e-05	240
PPD vs Temperature	0.8837	-4.7337	137.7905	3.63e-113	240
PPD vs RH	0.0015	0.0935	46.8877	0.546	240

Note: PMV-PPD regression is not included as an independent statistical relationship because PPD is analytically derived from PMV using the standard ISO/Fanger equation. Any PMV-PPD plot is therefore used only as a consistency check.

Table 7. Descriptive statistics of thermal comfort and environmental parameters (n = 240)

Parameter	Mean	Standard deviation	Minimum	Maximum
PMV	-1.248	1.291	-3.698	1.332
PPD (%)	50.080	34.899	5.000	99.900
Temperature (°C)	18.529	6.930	5.742	30.000
Relative humidity (%)	34.152	14.620	4.676	67.187
Air velocity (m/s)	0.112	0.099	0.008	0.569

Fig. 15a. (PMV vs PPD). The plot shows the analytical relationship between PMV and PPD for the simulated comfort dataset. Predicted dissatisfaction is lowest near thermal neutrality and increases as PMV moves away from zero, particularly towards cooler discomfort in the present dataset. Since PPD is derived directly from PMV using the standard ISO/Fanger relationship, this plot is presented as a consistency check of the comfort-index calculation rather than as an independent empirical regression. The seasonal colouring highlights how summer and winter cases are distributed along the same PMV-PPD relationship.

Fig. 15b. (PMV vs air temperature). This is the clearest relationship in the dataset: PMV increases with air temperature, with the regression accounting for most of the variation ($R^2 \approx 0.92$). The comfort band around $-0.5 \leq \text{PMV} \leq 0.5$ highlights where conditions are near neutral; open and closed window cases follow the same overall trend.

Fig. 15c. (PMV vs relative humidity). Humidity shows almost no linear effect on PMV. The regression is essentially flat ($R^2 \approx 0.02$), and PMV values are spread across a narrow RH range, indicating little explanatory power from humidity in these conditions.

Fig. 15d. (PMV vs air velocity). Air velocity has a weak negative association with PMV ($R^2 \approx 0.07$): higher speeds tend to correspond to slightly cooler perceived conditions, but the scatter is large and the trend explains only a small portion of the variability.

Fig. 15e. (PPD vs air temperature). As air temperature rises, predicted dissatisfaction falls, the fitted model captures most of the variation ($R^2 \approx 0.88, n = 240$). The 10% reference line shows many observations sit above commonly used

dissatisfaction thresholds, and both open- and closed-window cases follow the same overall pattern.

Fig. 15f. (PPD vs relative humidity). Relative humidity has virtually no linear relationship with PPD in these data ($R^2 \approx 0.0015$). Points are widely scattered and the regression line offers little explanatory power, so humidity is a poor predictor of dissatisfaction here.

Fig 16. (Vertical temperature stratification). Closed windows produce relatively uniform vertical temperatures, while open windows lead to much stronger stratification, especially in winter. Stratification is noticeably larger with windows open, and one sensor (m3-ankle) stands out as an outlier.

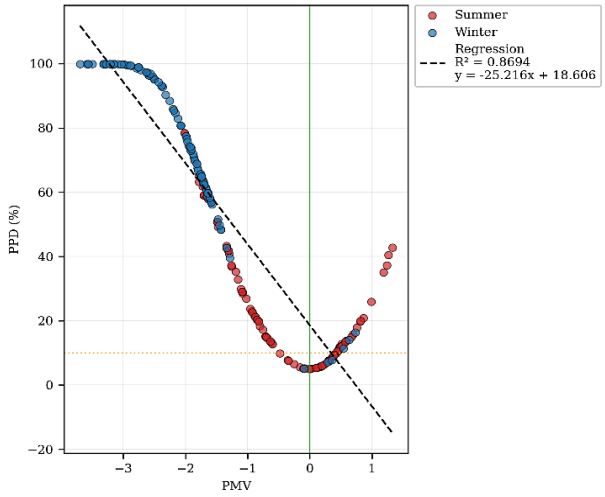

Fig. 15a. PMV vs PPD

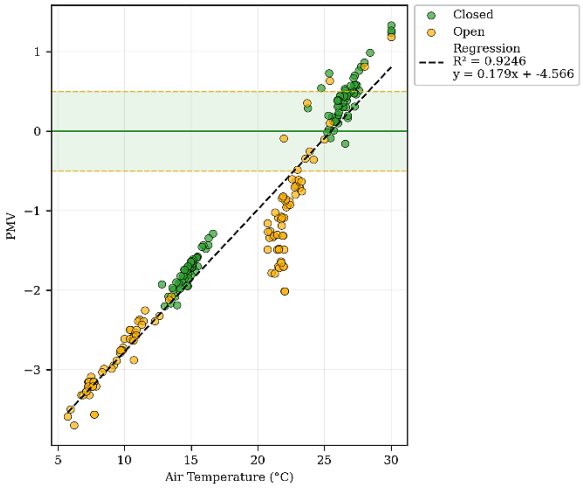

Fig. 15b. PMV vs Air Temperature

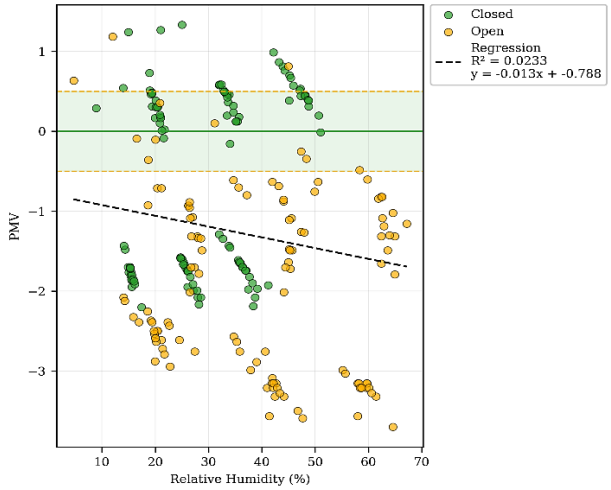

Fig. 15c. PMV vs Relative Humidity

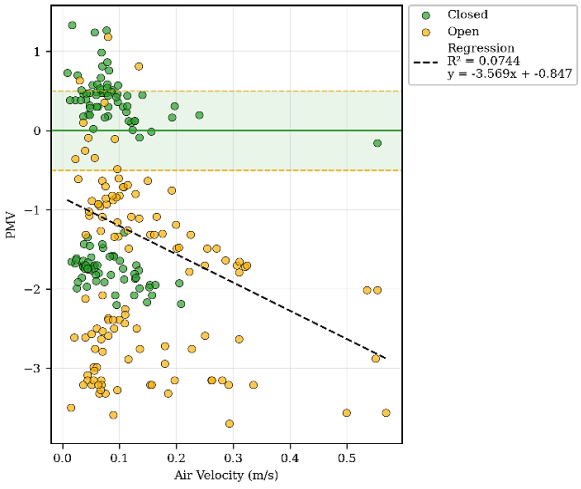

Fig. 15d. PMV vs Air Velocity

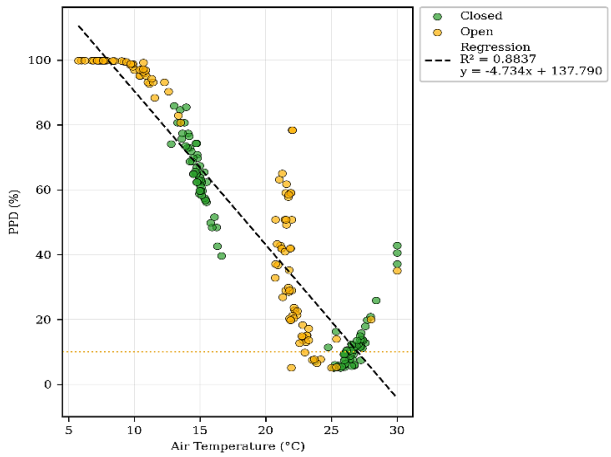

Fig. 15e. PPD vs Air Temperature

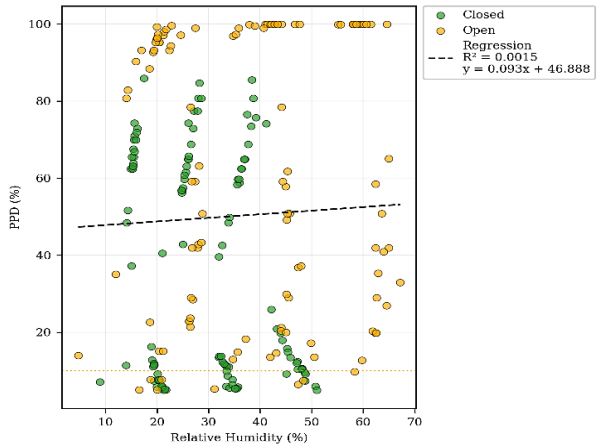

Fig. 15f. PPD vs Relative Humidity

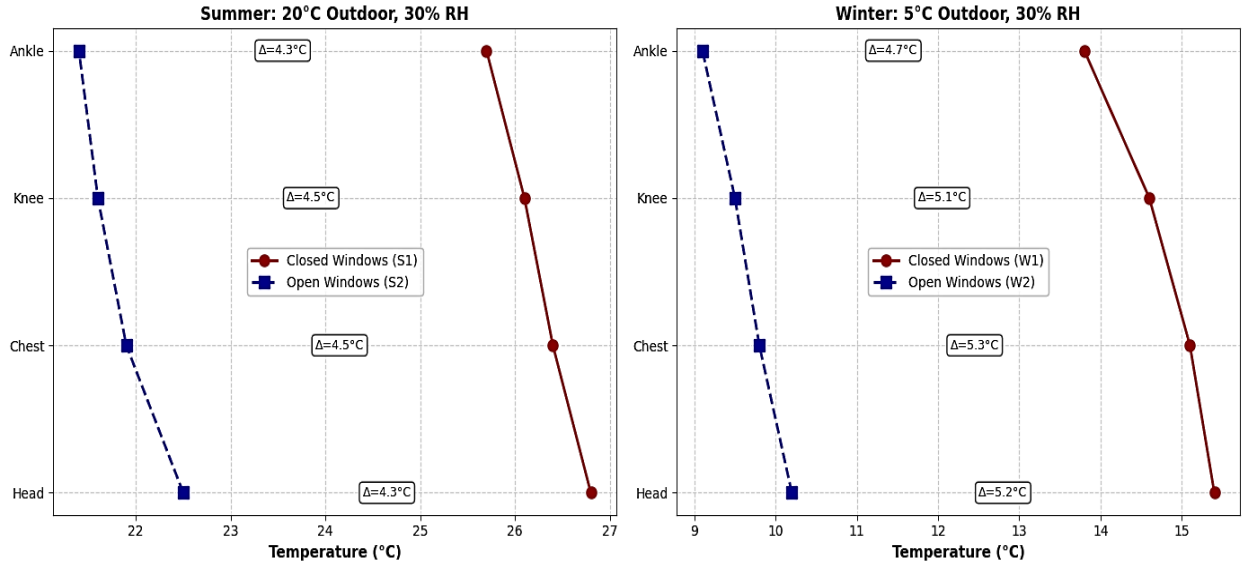

Fig 16. Vertical Temperature Stratification by window state

E. ZONE-BY-ZONE THERMAL COMFORT ANALYSIS

Table 8 shows zonal comfort analysis for the five locations of the mannequin, which shows significant spatial differences. The zonal analysis reveals obvious differences in areas of the house. The stair landing (m3) is the most variable with the greatest temperature differences between the states that the window is open and closed. The bedrooms (m4 and m5), on the other hand, generally maintain slightly better comfort during the summer but are more exposed to heat loss during the winter, which means less favourable conditions when it is cold outside. The living area (m1) is under most conditions in a moderate range, but in the case of winter with the windows open, there is an association with noticeable thermal discomfort.

Table 8. Zonal Thermal Comfort Analysis (Average PMV by Location)

Mannequin	Location	Summer Closed	Summer Open	Winter Closed	Winter Open
m1	Living Room	0.48	-1.31	-1.55	-2.21
m2	Kitchen	0.51	-1.22	-1.58	-2.18
m3	Stair Landing	0.42	-1.35	-1.47	-2.15
m4	Bedroom 1	0.53	-1.28	-1.61	-2.23
m5	Bedroom 2	0.49	-1.19	-1.59	-2.19

F. HUMIDITY EFFECTS ON THERMAL COMFORT

Fig. 17. shows that changing relative humidity from about 30% to 70% only slightly alters thermal sensation compared with the much larger effects of season and whether windows are open.

In summer with windows closed, PMV rises a little as humidity increases (about $0.48 \rightarrow 0.58$), a small shift toward feeling warmer. With windows open in summer, PMV stays near -1.3, with only a shallow dip around 50% RH. In winter, PMV is cooler overall: closed windows drop slightly (about $-1.52 \rightarrow -1.62$) and open windows remain around -2.2.

The PPD plot on the right tells the same narrative. Humidity moves dissatisfaction by only a few percentage points within each case, while season and window state make the biggest difference. For example, summer closed rises a little ($\approx 12\% \rightarrow 15\%$), summer open stays near 42%, winter closed increases slightly ($\approx 53\% \rightarrow 57\%$), and winter open remains very high (low- to mid-80s).

Overall, humidity has a minor, secondary effect; season and whether windows are open dominate comfort outcomes.

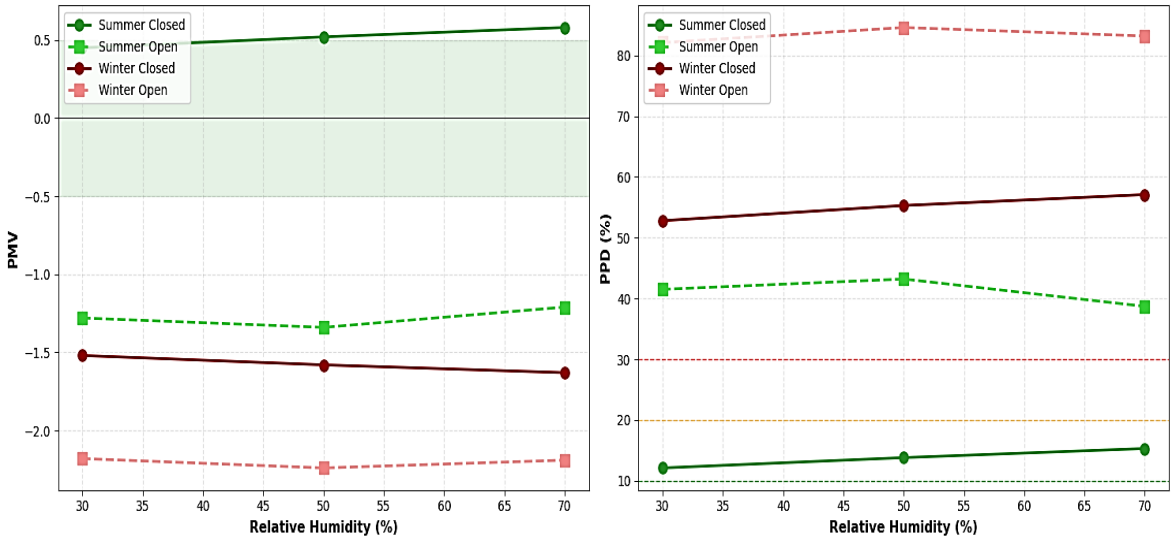

Fig. 17. Impact of Relative Humidity on Thermal Comfort

IV. DISCUSSION

A. INTERPRETATION OF THERMAL COMFORT FINDINGS

Using standard physiological assumptions (met = 1.4 and seasonal clothing levels) gives a more consistent and realistic assessment of radiator performance, in line with studies showing that personal factors strongly influence PMV/PPD outcomes [18][19].

In summer, the closed-window cases (S1, S3, S5) remained slightly warm but close to acceptable comfort, with PMV values of about 0.48-0.58 and PPD of 12-15%. This suggests that the system can maintain broadly reasonable comfort when heat is retained indoors.

The summer open-window cases (S2, S4, S6) performed worse, with PMV dropping to -1.21 to -1.34 and PPD rising above 38%, showing the strong cooling effect of ventilation heat loss. This is consistent with studies indicating that open-window ventilation does not always ensure comfort in temperate European climates [20][21].

Winter showed the greatest limitation. Even with windows closed, cases W1, W3 and W5 remained too cold (PMV -1.52 to -1.63; PPD above 52%), indicating insufficient radiator heating under winter conditions. The winter open-window cases (W2, W4, W6) were much worse, with PMV below -2.18 and PPD above 82%, well outside acceptable residential comfort limits [22].

B. INTERPRETATION OF STATISTICAL ANALYSIS

The regression results support the physical interpretation of the CFD outcomes, but they should be framed carefully. Air temperature showed the strongest relationship with both PMV and PPD, which is consistent with the large temperature spread across the scenarios and with earlier studies showing that air or operative temperature explains most of the variation in thermal comfort response [23][24]. However, this strong PMV-air-temperature relationship should also be interpreted considering the MRT treatment adopted in this study. Since the CFD model did not solve radiative heat exchange, local air temperature was used as the proxy for mean radiant temperature in the PMV calculation. As a result, the PMV response is expected to be strongly temperature-driven, and the high PMV-air-temperature association should not be interpreted as evidence that radiant effects are unimportant. Rather, it reflects the structure of the present comfort calculation, in which unresolved radiant asymmetry is not independently represented.

By contrast, humidity and air velocity contributed only weak linear trends, indicating that their influence was relatively small under the present conditions [25][26][27]. The PMV-PPD relationship, although strong, should not be presented as an independent empirical finding because PPD is derived directly from PMV, even though the observed curved trend remains consistent with the standard non-linear PMV-PPD relationship used in comfort standards [23][25]. In addition, because the 240 observations are nested within scenarios, locations and body heights, the regression output should be interpreted descriptively rather than as strong inferential statistics. This limitation is particularly relevant in winter cases and near windows or radiator surfaces, where differences between air temperature and mean radiant temperature may be more pronounced.

C. IMPORTANCE OF SPATIAL NON-UNIFORMITY

A major contribution of the CFD analysis is the prediction of strong spatial non-uniformity across the house. The

stair/landing region, particularly the m3-ankle position, repeatedly behaved differently from the main occupied zones within the CFD results. This indicates that whole-house comfort may not be represented adequately by a single temperature setpoint or by a single central measurement location. Even where average room conditions appear moderate, local discomfort may still occur because of stratification, weak mixing and transitional flow behaviour [28].

The repeated warm condition at the m3-ankle point should not be interpreted simply as a numerical or statistical outlier. Its location within the stairs/landing region places it in a transitional vertical zone where buoyancy-driven flow can differ substantially from the main rooms. Warm air generated by the lower-floor radiators rises naturally through the stair opening, creating a stack-effect-like upward exchange between the lower and upper levels. As this buoyant flow enters the stair/landing volume, local recirculation and weak lateral mixing can cause heat to accumulate near the landing and adjacent boundary surfaces. This provides a plausible physical explanation for why the m3-ankle point remained warmer than surrounding occupied-zone locations across several scenarios.

The stair/landing anomaly is therefore not merely a statistical outlier within the CFD dataset; it represents a physically meaningful and control-relevant predicted zone within the house. This finding supports the need for zonal sensing and control strategies that account for vertical coupling, buoyancy-driven heat transport and local heat accumulation in multi-level radiator-heated dwellings. However, because full-field experimental validation was not performed, the spatial anomaly should be interpreted as a CFD-predicted thermal feature supported by limited point-based validation rather than as a fully experimentally verified full-domain phenomenon.

D. ROLE OF HUMIDITY RELATIVE TO TEMPERATURE

Within the tested range, relative humidity had only a weak linear association with PMV and PPD compared with temperature. This does not mean that humidity is irrelevant, but rather that its effect was secondary in relation to the much larger thermal shifts produced by outdoor temperature and window opening. This interpretation is consistent with recent domestic indoor comfort modelling work, where humidity was considered alongside radiator surface temperature, ventilation and seasonal conditions rather than treated as an isolated primary driver [14]. In practical terms, this suggests that humidity may be included as a supporting comfort variable in control logic, but the main control sensitivity in this study lies in maintaining temperature and managing ventilation events.

E. INFLUENCE OF OUTDOOR BOUNDARY TEMPERATURE SELECTION

The seasonal outdoor temperatures of 20 °C and 5 °C were selected as representative controlled boundary conditions for the summer and winter scenario groups, respectively. The purpose was not to perform a full outdoor-temperature sensitivity analysis, but to compare the effects of season, window state and humidity under fixed and interpretable seasonal boundaries. Different outdoor temperatures would be expected to shift the absolute PMV and PPD values, particularly in winter where heat loss through the envelope and openings is more pronounced. However, the present results still provide useful comparative insight into how the radiator system responds to ventilation and humidity effects under representative seasonal conditions.

F. IMPLICATION FOR SMART RADIATOR CONTROL

The findings support a comfort-informed control approach in which window-state awareness and zonal operation are prioritised, rather than reliance on fixed temperature setpoints alone. This is consistent with recent smart-building studies that advocate multi-parameter, comfort-focused control strategies [19].

The strongest and most consistent deterioration in comfort occurred when windows were open, especially in winter, showing that ventilation events dominate control performance in this dwelling. Likewise, the persistent stair/landing anomaly indicates that transitional areas may require separate treatment from primary occupied zones through zonal or occupancy-responsive control. By contrast, humidity appears better suited to a secondary or corrective role than to a primary control target within the range studied here, while dynamic adjustment of comfort assumptions, including clothing-related effects, has also been shown to improve comfort prediction in building control studies [19]. These implications are consistent with the evidence presented, while optimisation of control schedules or emitter sizing remains outside the scope of the present paper.

G. LIMITATIONS

This study is based on a single smart-home testbed and one whole-house radiator layout comprising seven hydronic radiators; therefore, direct generalisation to other dwelling types, emitter layouts, radiator sizes and climates should be made cautiously. PMV and PPD were used as standard overall comfort indicators, but they remain steady-state indices applied to a thermally non-uniform indoor environment.

Radiative heat transfer was not explicitly solved in the CFD model. The radiators were represented as isothermal heating surfaces, with their effect captured through convective heat transfer and buoyancy-driven airflow. Surface-to-surface long-wave radiation exchange between radiators, glazing, walls and mannequin surfaces was therefore not resolved, and mean radiant temperature was approximated using local air temperature in the PMV/PPD calculation. The results should therefore be interpreted as comparative air-temperature-based comfort trends rather than full radiant-comfort or radiant-asymmetry predictions.

The RNG k-ε model with enhanced wall treatment was selected for robustness and computational practicality in whole-house transient simulations. However, as a two-equation RANS model, it may not fully resolve low-Reynolds-number transitional behaviour, turbulence anisotropy, local separation or detailed cold-window downdraught structures. Future work should assess turbulence-model sensitivity using SST k-ω, transitional SST, LES or hybrid RANS-LES approaches.

Although all scenarios were simulated in transient mode using time-varying inlet forcing, comfort results were extracted from the final simulated time step only. Experimental comparison was also limited to discrete body-height measurements in two closed-window summer scenarios. Therefore, winter, open-window and full-domain spatial fields should be interpreted as comparative CFD predictions within an experimentally supported modelling framework, rather than as fully experimentally validated fields. Future work should include full-field or higher-density validation methods, such as Background Oriented Schlieren, infrared thermography,

particle image velocimetry or dense sensor mapping.

Finally, the outdoor temperatures of 20 °C and 5 °C were selected as representative seasonal boundary conditions, not as a full outdoor-temperature sensitivity study. The present study was therefore designed to compare radiator performance under controlled seasonal, ventilation and humidity conditions rather than to perform full climate sensitivity analysis.

H. PRACTICAL IMPLICATIONS FOR SMART-HOME HEATING

The present results suggest several practical implications for radiator-heated smart homes. First, window-state awareness is likely to provide the greatest control benefit, since comfort deteriorated sharply whenever windows were opened. Second, the observed stair/landing anomaly shows that transitional spaces should not be assumed to behave like the main living zones; zonal control or targeted balancing may therefore be required. Third, humidity may be incorporated as a supporting comfort input, but the present results do not justify making it the primary control variable.

Finally, the winter results suggest that the installed radiator system and its heat distribution pattern may be insufficient to maintain comfort under higher heat-loss conditions. These implications are broadly consistent with recent smart-building research on comfort-informed and adaptive heating control, although any change in radiator sizing or control schedule should still be confirmed through building-specific heat-loss assessment rather than inferred as a universal rule from this study alone [19].

I. DIGITAL-TWINS AND AUGMENTED REALITY (AR) VISUALISATION PATHWAY

Although the present study focuses on CFD-based comfort assessment rather than real-time system deployment, the generated spatial thermal fields provide a direct basis for future smart-home digital-twin and AR visualisation. In a practical implementation, CFD-derived temperature, velocity and comfort fields could be reduced into zone-level comfort maps, linked to live sensor nodes, and displayed through a digital-twin interface or AR overlay. This would allow users or control systems to identify local thermal anomalies, such as the stair/landing overheating observed in this study, in a more intuitive spatial format. However, the development of real-time AR algorithms, user-interface design and closed-loop terminal control is outside the scope of the present paper and should be addressed in future work.

V. CONCLUSION

This study assessed the thermal comfort performance of a conventional hydronic radiator system in the Huddersfield Smart House using a whole-house transient CFD framework and PMV/PPD-based comfort analysis. Twelve controlled scenarios were examined using representative summer and winter outdoor boundary temperatures of 20 °C and 5 °C, respectively, combined with two window states and three relative humidity levels. Point-based comparison against experimental PMV and PPD measurements for two closed-window summer scenarios showed close agreement, supporting the use of the model for comparative comfort assessment under the measured conditions.

Across the scenario set, the radiator system produced slightly warm but near-neutral conditions in summer when windows were closed, whereas opening the windows shifted the indoor environment into cool discomfort even under summer boundary

conditions. In winter, the system remained unable to maintain acceptable comfort even with windows closed, and open-window operation produced severe cold discomfort. Air temperature was the dominant driver of comfort trends within the adopted air-temperature-based MRT approximation, while relative humidity showed only a weak linear association within the tested range. CFD-based spatial analysis indicated vertical stratification and a persistent thermal anomaly in the stair/landing region, demonstrating that whole-house comfort may not be represented adequately by a single setpoint or a single average condition. The persistent m3-ankle anomaly was physically linked to buoyancy-driven warm-air transport through the stairwell and local heat pooling near the landing, highlighting the importance of accounting for vertical coupling in multi-level smart-home comfort assessment.

Overall, the study provides a CFD-based framework for scenario-end-state assessment of thermal comfort in a radiator-heated smart-home testbed. The findings support the importance of window-state awareness, zonal interpretation and spatial comfort mapping in smart-home heating control. However, they should be interpreted within the validation and modelling boundaries of the study, particularly the limited point-based validation, the absence of full-field experimental validation of the predicted spatial flow structures, the air-temperature-based approximation of mean radiant temperature, the absence of explicit surface-to-surface radiation modelling, and the use of a two-equation RANS turbulence closure. Optimisation of emitter sizing, real-time control rules and AR-based digital-twin implementation remain outside the scope of the present work.

CONFLICT OF INTEREST STATEMENT

The authors confirm that there are no conflicts of interest related to this work.

References

[1] Q. Wu, W. Xu, Y. Zhu, and J. Liu, "Optimization for the temperature range of radiator for preventing draught risk of cold window," *Energy Build.*, vol. 323, p. 114815, Nov. 2024, doi: 10.1016/j.enbuild.2024.114815.

[2] A. Bueno, A. De Paula Xavier, and E. Broday, "Evaluating the Connection between Thermal Comfort and Productivity in Buildings: A Systematic Literature Review," *Buildings*, vol. 11, no. 6, p. 244, Jun. 2021, doi: 10.3390/buildings11060244.

[3] P. Nejat, F. Jomehzadeh, M. M. Taheri, M. Gohari, and M. Z. Abd. Majid, "A global review of energy consumption, CO 2 emissions and policy in the residential sector (with an overview of the top ten CO 2 emitting countries)," *Renew. Sustain. Energy Rev.*, vol. 43, pp. 843–862, Mar. 2015, doi: 10.1016/j.rser.2014.11.066.

[4] "Buildings - Energy System," IEA. Accessed: Jan. 27, 2026. [Online]. Available: https://www.iea.org/energy-system/buildings

[5] B. W. Olesen, "International standards for the indoor environment," *Indoor Air*, vol. 14, no. s7, pp. 18–26, Aug. 2004, doi: 10.1111/j.1600-0668.2004.00268.x.

[6] A. L. Slimani, S. Mazouz, and S. Nekhila, "Computational Fluid Dynamics-Based Quantitative Assessment and Performance Optimization of Thermal Comfort in Hyper-Arid Climate Office Buildings," *Sustainability*, vol. 17, no. 22, p. 10229, Nov. 2025, doi: 10.3390/su172210229.

[7] K.-V. Võsa, A. Ferrantelli, and J. Kurnitski, “A combined analytical model for increasing the accuracy of heat emission predictions in rooms heated by radiators,” *J. Build. Eng.*, vol. 23, pp. 291–300, May 2019, doi: 10.1016/j.jobe.2019.02.009.

[8] R. Gulzar *et al.*, “Evaluation of thermal comfort in a smart house heated by a modern storage radiator,” in *Proceedings of the International Conference on Maintenance and Intelligent Asset Management: ICMIAM 2023*, Asset Management Council of Australia, Dec. 2023, pp. 48–53. Accessed: May 14, 2026. [Online]. Available: https://pure.hud.ac.uk/en/publications/evaluation-of-thermal-comfort-in-a-smart-house-heated-by-a-modern/

[9] Q. Wu, Z. Wang, J. Dong, and J. Liu, “A method for judging the overheating of the radiator in the compensation of window downdraught based on thermal image velocimetry,” *Build. Environ.*, vol. 197, p. 107858, Jun. 2021, doi: 10.1016/j.buildenv.2021.107858.

[10] A. Isiyaku, R. Mishra, A. Aliyu, and F. Jackson, “Influence of Radiator Operation on Indoor Air Dynamics in the Huddersfield Smart House: A Computational Analysis,” in *Proceedings of the International Conference on Maintenance and Intelligent Asset Management: ICMIAM 2023*, Asset Management Council of Australia, Dec. 2023, pp. 66–71. Accessed: May 14, 2026. [Online]. Available: https://pure.hud.ac.uk/en/publications/influence-of-radiator-operation-on-indoor-air-dynamics-in-the-hud/

[11] G. A. Ganesh, S. L. Sinha, V. Panchore, and T. N. Verma, “CFD analysis of natural ventilation’s role in modulating transient metabolic rate and enhancing indoor comfort,” *Energy Sources Part Recovery Util. Environ. Eff.*, vol. 47, no. 1, pp. 4941–4958, Jun. 2025, doi: 10.1080/15567036.2025.2462274.

[12] D. Markov *et al.*, “On the Procedure of Draught Rate Assessment in Indoor Spaces,” *Appl. Sci.*, vol. 10, no. 15, p. 5036, Jul. 2020, doi: 10.3390/app10155036.

[13] B. Zhou, Z. Li, B. Yang, X. Li, F. Wang, and S. Wei, “Thermal and draught perception in fluctuating stratified thermal environments with intermittent impinging jet ventilation,” *Build. Environ.*, vol. 229, p. 109934, Feb. 2023, doi: 10.1016/j.buildenv.2022.109934.

[14] S. O. Sogbaike *et al.*, “Optimal thermal comfort quantification in domestic indoor spaces under varying ambient and seasonal conditions – a numerical approach,” *Adv. Build. Energy Res.*, vol. 19, no. 6, pp. 718–745, Nov. 2025, doi: 10.1080/17512549.2025.2540900.

[15] A. Laouadi, “Development of a radiant heating and cooling model for building energy simulation software,” *Build. Environ.*, vol. 39, no. 4, pp. 421–431, Apr. 2004, doi: 10.1016/j.buildenv.2003.09.016.

[16] M. Bojić, D. Cvetković, V. Marjanović, M. Blagojević, and Z. Djordjević, “Performances of low temperature radiant heating systems,” *Energy Build.*, vol. 61, pp. 233–238, Jun. 2013, doi: 10.1016/j.enbuild.2013.02.033.

[17] C. Chillon Geck, T. H. M. Al-Zuriqat, H. Alsaad, C. Völker, and K. Smarlsy, “Automated thermal comfort monitoring using IoT technologies,” presented at the 2023 European Conference on Computing in Construction and the 40th International CIB W78 Conference, Jul. 2023. doi: 10.35490/EC3.2023.195.

[18] A. Schieweck *et al.*, "Smart homes and the control of indoor air quality," *Renew. Sustain. Energy Rev.*, vol. 94, pp. 705–718, Oct. 2018, doi: 10.1016/j.rser.2018.05.057.

[19] A. E. Isiyaku, M. Aderibigbe, R. Mishra, and A. Gaur, "Performance Evaluation of Smart Home Digital Twins: A Thermal Comfort Case Study," *J. Dyn. Monit. Diagn.*, Mar. 2026, doi: 10.37965/jdmd.2026.1133.

[20] V. Tuninetti, B. Ales, and T. Mora Chandía, "Numerical and Experimental Analysis of Thermal Stratification in Locally Heated Residential Spaces," *Buildings*, vol. 15, no. 14, p. 2417, Jul. 2025, doi: 10.3390/buildings15142417.

[21] S. B. Pope, "Turbulent Flows," Cambridge Aspire website. Accessed: Jun. 02, 2026. [Online]. Available: https://www.cambridge.org/highereducation/books/turbulent-flows/69322053C06F73F7EB7124915F9256BD

[22] H. K. Versteeg and W. Malalasekera, *An introduction to computational fluid dynamics: the finite volume method*, 2. ed., [Nachdr.]. Harlow: Pearson/Prentice Hall, 2007.

[23] "Ansys Help." Accessed: Jun. 02, 2026. [Online]. Available: https://ansyshelp.ansys.com/account/secured?returnurl=/Views/Secured/main_page.html

[24] V. Yakhot, S. A. Orszag, S. Thangam, T. B. Gatski, and C. G. Speziale, "Development of turbulence models for shear flows by a double expansion technique," *Phys. Fluids Fluid Dyn.*, vol. 4, no. 7, pp. 1510–1520, Jul. 1992, doi: 10.1063/1.858424.

[25] "Procedure for Estimation and Reporting of Uncertainty Due to Discretization in CFD Applications," *J. Fluids Eng.*, vol. 130, no. 7, Jul. 2008, doi: 10.1115/1.2960953.

[26] F. Stern, R. V. Wilson, H. W. Coleman, and E. G. Paterson, "Verification and Validation of CFD Simulations:," Defense Technical Information Center, Fort Belvoir, VA, Sep. 1999. doi: 10.21236/ADA458015.

[27] H. Schlichting and K. Gersten, *Boundary-Layer Theory*. Berlin, Heidelberg: Springer Berlin Heidelberg, 2017. doi: 10.1007/978-3-662-52919-5.

[28] Accessed: Jan. 27, 2026. [Online]. Available: https://www.iea.org/energy-system/buildings

[29] T. Cheung, S. Schiavon, T. Parkinson, P. Li, and G. Brager, "Analysis of the accuracy on PMV – PPD model using the ASHRAE Global Thermal Comfort Database II," *Build. Environ.*, vol. 153, pp. 205–217, Apr. 2019, doi: 10.1016/j.buildenv.2019.01.055.

[30] J. Liu, I. W. Foged, and T. B. Moeslund, "Clothing Insulation Rate and Metabolic Rate Estimation for Individual Thermal Comfort Assessment in Real Life," *Sensors*, vol. 22, no. 2, p. 619, Jan. 2022, doi: 10.3390/s22020619.

[31] S. Carlucci, L. Bai, R. De Dear, and L. Yang, "Review of adaptive thermal comfort models in built environmental regulatory documents," *Build. Environ.*, vol. 137, pp. 73–89, Jun. 2018, doi: 10.1016/j.buildenv.2018.03.053.

[32] D. Bienvenido-Huertas, J. A. Pulido-Arcas, C. Rubio-Bellido, and A. Pérez-Fargallo, "Feasibility of adaptive thermal comfort for energy savings in cooling and heating: A study on Europe and the Mediterranean basin," *Urban Clim.*, vol. 36, p. 100807, Mar. 2021, doi: 10.1016/j.uclim.2021.100807.

[33] B. Jeong, "Assessing indoor air temperature settings in residential

buildings during the COVID-19 era," *Build. Environ.*, vol. 265, p. 112034, Nov. 2024, doi: 10.1016/j.buildenv.2024.112034.

[34] J.-H. Kim, Y.-K. Min, and B. Kim, "Is the PMV Index an Indicator of Human Thermal Comfort Sensation?," *Int. J. Smart Home*, vol. 7, no. 1, 2013.

[35] "Standard 55 – Thermal Environmental Conditions for Human Occupancy." Accessed: Jan. 31, 2026. [Online]. Available: https://www.ashrae.org/technical-resources/bookstore/standard-55-thermal-environmental-conditions-for-human-occupancy